NAR Cancer, 2025, **7**, zcaf007
https://doi.org/10.1093/narcan/zcaf007
Cancer Computational Biology

OXFORD

Harnessing transcriptional regulation of alternative end-joining to predict cancer treatment

Roderic Espín[1,2], Ferran Medina-Jover[1,2,3,†], Javier Sigüenza-Andrade[1,2,†], Sònia Farran-Matas[1,2,†], Francesca Mateo[1,2,†], Agnes Figueras[1,2], Rosario T. Sanz[4], Guillermo Pablo Vicent[4], Arzoo Shabbir[1,2], Lara Ruiz-Auladell[1,2], Emilio Racionero-Andrés[1], Irene García[1,2], Alexandra Baiges[1,2], Lídia Franco-Luzón[1,2], Adrián Martínez-Tebar[1,2], Miguel Angel Pardo-Cea[1,2], María Martínez-Iniesta[1,2], Xieng Chen Wang[1,2], Elisabet Cuyàs[1,5], Javier A. Menendez[1,5], Marta Lopez-Cerda[2], Purificacion Muñoz[2], Ivonne Richaud[6,7], Angel Raya[6,7,8], Isabel Fabregat[2,9], Alberto Villanueva[1,2], Xènia Serrat[10], Julián Cerón[10], Montserrat Alemany[2,11], Inés Guix[12], Andrea Herencia-Ropero[13,14], Violeta Serra[14], Rehna Krishnan[15], Karim Mekhail[16], Razqallah Hakem[15,17], Jordi Bruna[2,11], Mary Helen Barcellos-Hoff[12,*], Francesc Viñals[1,2,3,*], Álvaro Aytes[1,2,*], Miquel Angel Pujana[1,2,5,*]

[1]ProCURE, Catalan Institute of Oncology, L'Hospitalet del Llobregat, Barcelona 08908, Spain
[2]Oncobell, Bellvitge Institute for Biomedical Research (IDIBELL), L'Hospitalet del Llobregat, Barcelona 08908, Spain
[3]Department of Physiological Sciences, University of Barcelona, L'Hospitalet del Llobregat, Barcelona 08908, Spain
[4]Molecular Biology Institute of Barcelona, Spanish National Research Council (IBMB-CSIC), Barcelona 08028, Spain
[5]Girona Biomedical Research Institute (IDIBGI), Salt, Girona 17190, Spain
[6]Regenerative Medicine Program and Program for Clinical Translation of Regenerative Medicine in Catalonia—P-CMR[C], Bellvitge Institute for Biomedical Research (IDIBELL), L'Hospitalet del Llobregat, Barcelona 08908, Spain
[7]Biomedical Research Network Centre in Bioengineering, Nanomaterials, and Nanomedicine (CIBER-BBN), Instituto de Salud Carlos III, Madrid 28029, Spain
[8]Catalan Institution for Research and Advanced Studies (ICREA), Barcelona 08010, Spain
[9]Biomedical Research Networking Centre in Hepatic and Digestive Diseases (CIBERehd), Instituto de Salud Carlos III, Madrid 28029, Spain
[10]Modeling Human Diseases in *C. elegans* Group, Genes, Diseases, and Therapies Program, Bellvitge Institute for Biomedical Research (IDIBELL), L'Hospitalet del Llobregat, Barcelona 08908, Spain
[11]Neuro-Oncology Unit, University Hospital of Bellvitge, Catalan Institute of Oncology, Bellvitge Institute for Biomedical Research (IDIBELL), L'Hospitalet del Llobregat, Barcelona 08908, Spain
[12]Department of Radiation Oncology and Helen Diller Family Comprehensive Cancer Centre, University of California San Francisco, San Francisco, CA 94115, United States
[13]Department of Biochemistry and Molecular Biology, Autonomous University of Barcelona, Barcelona 08193, Spain
[14]Experimental Therapeutics Group, Vall d'Hebron Institute of Oncology (VHIO), Vall d'Hebron Barcelona Hospital Campus, Barcelona 08035, Spain
[15]Princess Margaret Cancer Centre, University Health Network, Toronto, ON M5G 2C1, Canada
[16]Department of Laboratory Medicine and Pathobiology, Temerty Faculty of Medicine, University of Toronto, Toronto, ON M5S 1A8, Canada
[17]Department of Medical Biophysics, University of Toronto, Toronto, ON M5S 1A8, Canada

[*]To whom correspondence should be addressed. Tel: +34 932 607 952; Email: mapujana@iconcologia.net
Correspondence may also be addressed to Mary Helen Barcellos-Hoff. Tel: +1 415 476 8091; Email: maryhelen.barcellos-hoff@ucsf.edu
Correspondence may also be addressed to Francesc Viñals. Tel: +34 932 607 952; Email: fvinyals@iconcologia.net
Correspondence may also be addressed to Álvaro Aytes. Tel: +34 932 607 952; Email: aaytes@idibell.cat
[†]These authors should be regarded as Joint Second Authors.

Abstract

Alternative end-joining (alt-EJ) is an error-prone DNA repair pathway that cancer cells deficient in homologous recombination rely on, making them vulnerable to synthetic lethality via inhibition of poly(ADP-ribose) polymerase (PARP). Targeting alt-EJ effector DNA polymerase theta (POLθ), which synergizes with PARP inhibitors and can overcome resistance, is of significant preclinical and clinical interest. However, the transcriptional regulation of alt-EJ and its interactions with processes driving cancer progression remain poorly understood. Here, we show that alt-EJ is suppressed by hypoxia while positively associated with MYC (myelocytomatosis oncogene) transcriptional activity. Hypoxia reduces *PARP1* and *POLQ* expression, decreases MYC binding at their promoters, and lowers PARylation and alt-EJ-mediated DNA repair in cancer cells. Tumors with

Received: October 17, 2024. **Revised:** February 13, 2025. **Editorial Decision:** February 14, 2025. **Accepted:** March 4, 2025

HIF1A mutations overexpress the alt-EJ gene signature. Inhibition of hypoxia-inducible factor 1α or *HIF1A* expression depletion, combined with PARP or POLθ inhibition, synergistically reduces the colony-forming capacity of cancer cells. Deep learning reveals the anticorrelation between alt-EJ and hypoxia across regions in tumor images, and the predictions for these and MYC activity achieve area under the curve values between 0.70 and 0.86. These findings further highlight the critical role of hypoxia in modulating DNA repair and present a strategy for predicting and improving outcomes centered on targeting alt-EJ.

Graphical abstract

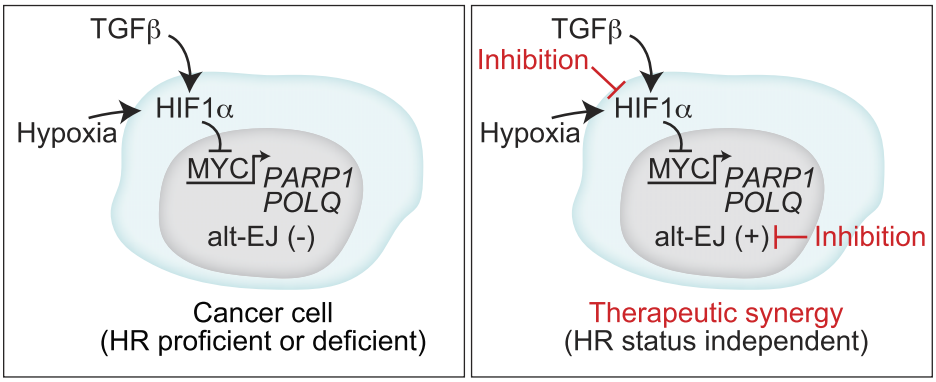

Introduction

Homologous recombination (HR) is a high-fidelity molecular mechanism crucial for accurately repairing double-strand breaks (DSBs) during the S and G2 phases of the cell cycle, when a sister chromatid is available as a template [1–3]. In cancer cells with defective HR—such as those with pathogenic variants in breast cancer gene 1 (*BRCA1*) or 2 (*BRCA2*) [4–6]—there is increased reliance on another DNA repair mechanism known as alternative end-joining (alt-EJ), also referred to as microhomology-mediated end-joining (MMEJ) [7–13]. This dependence forms the basis of the synthetic lethality exploited by inhibition of poly(ADP-ribose) polymerase (PARP) [7, 8], a strategy that has revolutionized cancer care [14]. Thus, assessing HR status has made PARP inhibition (PARPi) a standard treatment strategy for managing various cancers, including those of the breast, pancreas, prostate, and ovary [15–21]. Targeting alt-EJ is being extended to combination therapies and complementary approaches, including inhibition of DNA polymerase theta (POLθ), a central effector of alt-EJ/MMEJ or theta-mediated end-joining [10, 13, 22–26]. Inhibition of POLθ is synthetically lethal with the loss of *BRCA1* or *BRCA2*, can synergize with PARPi, and can also be applied to target cancer cells that developed resistance to PARPi [10, 23, 24]. However, our understanding of the transcriptional regulation of alt-EJ genes, particularly in the context of tumorigenic processes influencing DNA repair, remains limited [9, 27, 28].

The pleiotropic cytokine transforming growth factor β (TGFβ) can enhance the expression of HR components and pathway functionality [29–34]. Gene expression signatures of TGFβ and alt-EJ competency are frequently found to be anticorrelated in tumors, in a cancer cell-autonomous manner [35]. Inhibition of TGFβ signaling induces alt-EJ even in cancer cells that are HR-proficient [33]. TGFβ inhibition results in HR deficit because TGFβ regulates *BRCA1* expression via miR182 and cells shift to alt-EJ [30, 33]. Notably, neither alt-EJ execution nor expression of alt-EJ genes (*LIG1*, *PARP1*, or *POLQ*) is miR-182-dependent, which mechanistically separates the effects of TGFβ on HR from those on alt-EJ [33, 35, 36]. Here, by analyzing functional gene modules in breast cancer, we demonstrate that TGFβ signaling suppresses alt-EJ via hypoxia-inducible factor 1α (HIF1α). Hypoxia downregulates the alt-EJ competency signature, including *PARP1* and *POLQ* genes, by altering MYC (myelocytomatosis oncogene) binding at the corresponding promoters. Hypoxia is associated with reduced alt-EJ activity, while HIF1α inhibition increases PARylation. Furthermore, inhibition of HIF1α or depletion of *HIF1A* expression, in combination with PARPi or POLθi, acts synergistically to reduce the colony-forming ability of cancer cells, including HR-proficient models. This inverse relationship between alt-EJ and hypoxia is applied in cancer treatment prediction by using deep learning of tumor pathology images. The approach provides a framework for classifying tumors based on alt-EJ, hypoxia, and MYC activity, offering novel insights into alt-EJ regulation and its potential for enhancing precision in cancer treatment and for advancing effective combination therapies.

Materials and methods

Gene expression and molecular datasets

Clinical and gene expression [RNA sequencing FPKM (fragments per kilobase of transcript per million mapped reads) UQ (upper quartile-normalized)] data from The Cancer Genome Atlas (TCGA) studies [37] were obtained from the Genomic Data Commons (GDC) Data Portal (https://portal.gdc.cancer.gov). The cancer types are named using the corresponding TCGA study abbreviations (https://gdc.cancer.gov/resources-tcga-users/tcga-code-tables/tcga-study-abbreviations). The pediatric and hematological cancer normalized gene-expression data (reads per kilobase per million mapped reads (RPKM)) were also downloaded from cBioPortal [38]. The HR-deficiency scores in TCGA breast cancer (BRCA) corresponded to the combination of loss of heterozygosity, telomeric allelic imbalance, and large-scale transitions, computed in the HRDsum score [39, 40]. The TCGA kidney renal clear cell carcinomas (KIRC) with driver mutations of *VHL* were identified from cBioPortal [38], based on OncoKB annotations [41]. The TCGA tumors with *HIF1A* mutations, including frameshift, missense, and nonsense mutations were also identified from cBioPortal [38]. The single-cell processed count matrices of cancer

cell lines induced to epithelial–mesenchymal transition (EMT) were downloaded from the Gene Expression Omnibus (GEO) reference GSE147405 [42]. The PRO-seq (Precision Run-On with sequencing) data of *HIF1A*$^{-/-}$ and wild-type (WT) HCT166 cells in normoxia and hypoxia were downloaded from the GEO reference GSE145567 [43]. The Cancer Cell Line Encyclopedia (CCLE) [44] gene expression data were downloaded from the DepMap [45] portal (https://depmap.org/portal/; version 22Q2). The drug sensitivity data were also obtained from the DepMap portal, including the half-maximal inhibitory concentration (IC_{50}) and area under the dose-response curve (AUCdrug) from the CCLE [46] (version 24Q2) and the IC_{50} values from the Genomics of Drug Sensitivity in Cancer (GDSC) screens [47–49] (release 8.1). PARP1 protein levels, as measured by mass spectrometry in the CCLE and GDSC cell lines, were obtained from the corresponding publications [50, 51]. The optimal number of cell line clusters was computed using the elbow method [52] and samples were clustered using the *kmean* function in R's *stats* package (version 4.3.1). The MYC protein expression values in cancer cell lines were downloaded from The Cancer Proteome Atlas portal (https://tcpaportal.org/tcpa/download.html; reverse phase protein array data, level 4) [53]. SPATA2 software [54] was used to analyze the spatial transcriptomic data of glioblastoma (GBM) [55] and gene signatures were computed using its *addGeneSet* function. Tissues with an average gene signature score <20% were excluded from the analysis.

Gene signature analysis

The TGFβ (genes $n = 50$) and alt-EJ (genes $n = 36$) signatures have previously been reported and functionally validated against mutational signatures and molecular markers [33, 35, 36]. The hypoxia signature consisted of a 15-gene set [56], which was the best-performing among a group of functionally related signatures [57]. The MYC signature (genes $n = 355$) was derived from a MYC-centered regulatory network independent of a pluripotency network [58]. The signature scores were computed using the single-sample GSEA algorithm calculated using GSVA software [59] (version 1.43.1).

Non-negative matrix factorization and machine learning

Non-negative matrix factorization (NMF) [60] was used for unsupervised data dimension reduction and pattern identification in the TCGA BRCA dataset [37, 61]. The original gene-by-tumor matrix was decomposed into the production of two low-rank non-negative matrices, a basic matrix W and a coefficient matrix H. A rank of matrix factorization, k, from 2 to 50, was examined to preserve the information of the input dataset. The reconstruction error was computed using the Frobenius norm of the deviation between the original matrix X and its approximation WH, expressed as $error = \|X - WH\|_F$. The latent features (rows of matrix H) were fed into a neural network with a structure comprising an input layer of the NMF ranks, two hidden layers, each composed of 128 neurons using a rectified linear unit activation function [62], a layer with a 0.5 dropout rate to mitigate overfitting [63], and an output layer that predicted the HRDsum score. The Adam optimizer [64] was used for training, with a learning rate of 0.001 and batch size of 32. A validation set consisting of 20% of the data was used to monitor overfitting during training. Early stopping with a patience of 10 epochs was employed to prevent overtraining [65]. Spearman correlations were calculated for the training and test datasets to assess the relationship between the predicted and real HRDsum scores [39, 40]. The SHAP (Shapley additive explanations) values were computed as described [66] to assess the importance of each gene module in the model, identifying the most positively and negatively influential sets. The rank of gene weights in each module was evaluated for associations with curated gene sets using the GSEA algorithm (version 4.2.3) [67] with the classic metric, accounting for the uncertain biological impact of gene weights in NMF modules, including those with noncontributory values (i.e. equal to 0).

Multivariate regression analysis

Nineteen cancer types from TCGA were included in the analysis. The ratio of alt-EJ to TGFβ signature scores was calculated and used as the dependent variable in the regression model. The following independent variables were included: age at diagnosis, cancer type, gender, tumor grade, normalized expression level of *HIF1A*, mutation status of *MYC* (genomic amplification: yes/no), HRDsum score [39, 40], and gene expression signature scores for hypoxia [56], MYC [58], and cell cycle phases (G1-S, S, G2, G2-M, and M-G1) [68]. Analogous analyses were conducted using expression levels of the cell proliferation marker *MKI67* instead of cell cycle phase scores. The interaction term between the hypoxia and MYC signatures was included. The model was computed using the *lm* function in R software (version 4.3.1).

Cell culture and molecular analyses

The 22Rv1, DU145, MCF10A, MDA-MB-231, PC3, and T-47D cells were obtained from the American Type Culture Collection. The OVCAR4 and A2780 cells were a gift from Thomas Hamilton (Fox Chase Cancer Center) and Josefa Giménez-Bonafé (University of Barcelona), respectively. The microarray gene expression data for the MCF10A cell line are available under the GEO reference GSE8240 [69]. PrimePCR™ SYBR® Green Assays (Bio-Rad) were used to assess the expression of the alt-EJ genes *PARP1* and *POLQ* in total RNA of MCF10A cells, and gene control was peptidylprolyl isomerase (*PPIA*). Supplementary Table S1 lists the primer sequences of all genes examined in this study and the TaqMan assays used for validation. Gene expression values were measured using real-time quantitative polymerase chain reaction (qPCR) assays and differences computed by the ΔΔCt method [70]. The antibodies used for western blot were as follows: anti-actin (clone AC-15; dilution 1:2500; Sigma–Aldrich Merck, catalog A5441); anti-HIF1α, (described elsewhere [71]; dilution 1:500); anti-PAR (clone AM80; dilution 1:1000; Merck Millipore, catalog Ab-1/AM80); anti-tubulin (clone B-5-1-2; dilution 1:2000; Sigma–Aldrich Merck, catalog T6079); and anti-vinculin (dilution 1:2000; Sigma–Aldrich Merck, catalog V9131).

Measurement of alt-EJ activity

U2OS GFP-reporter cells (a gift from Prof. J. Stark) were employed to measure alt-EJ repair of I-*Sce*I-induced DSBs [72]. The cells were cultured in Dulbecco's modified Eagle's medium (DMEM) medium supplemented with 10% fetal bovine serum (FBS) and standard antibiotics, in an atmosphere of 95% air and 5% CO_2 at 37°C, or in physiological hypoxia, as detailed below. For the assays, 50 000 cells/well were seeded in 24-well plates and transfected the next day with an I-*Sce*I

expression plasmid (pCBA*Sce*I; Addgene, catalog 26477) using Lipofectamine 2000 (Thermo Fisher Scientific) according to the manufacturer's instructions. The transfection medium was replaced after 3 h with fresh DMEM 10% FBS and the cells were left for 24 h in normoxic or hypoxic conditions (21% versus 2% O_2; hypoxia using Whitley H35 Hypoxystation, Don Whitley Scientific). The wells for the hypoxic conditions were treated with medium plus dimethylsulfoxide (DMSO) or PX-478 (5 μM). The cells were trypsinized, washed with phosphate-buffered saline (PBS), fixed with 10% formaldehyde, and analyzed for GFP positivity using a MACSQuant Analyzer 16 Flow Cytometer. Singlet cells were gated by plotting forward scatter height against forward scatter area. A logarithmic plot of the gated cells was obtained using PE-A (yellow fluorescence, *X*-axis) and FITC-A (green fluorescence, *Y*-axis). Untransfected cells were used to detect autofluorescence.

Colony-forming cell assays and drug synergism

Colony-forming cell (CFC) assays were performed in a 12-well format using the following cell seeding numbers: 22Rv1, 500 cells; A2780, 800 cells; DU145, 200 cells; MDA-MB-231, 300 cells; OVCAR4, 1000 cells; PC3, 300 cells; and T47D, 1500 cells. For high-density seeding, a 20-fold increase in cell counts was applied. In the assays, we evaluated the inhibitory effects of monotherapy and specified drug combinations, including novobiocin (100 μM), olaparib (2 μM), PX-478 (5 μM), rucaparib (2 μM), and talazoparib (1 nM). Cells were treated with the indicated drugs every 24–48 h and cultured for 6–10 days. After treatment, cells were washed with PBS, stained with crystal violet solution, and thoroughly rinsed with tap water. Image acquisition was performed using QuPath software (version 0.5.0). The script for image analysis and Bliss synergy scoring [73] has been deposited on Zenodo and is available at https://doi.org/10.5281/zenodo.14885044. Two-tailed Student's unpaired *t*-test was used to assess the significance of the difference between control and treatment groups, with values of $P < .05$ considered significant. The Bliss independence model [73] assumes that two given drugs produce their effects independently and that significant deviation from their multiplicative effect indicates antagonism or synergism. We implemented the Bliss synergy score from the SynergyFinder [74]. A bootstrapping resampling method was applied to estimate the 95% confidence interval (CI). A score of 10 was interpreted as a 10% response beyond expectation. Dose-response viability matrices were used to evaluate the combination of PX-478 (1.5–40 μM) and rucaparib (2.5–80 μM) over 72 h, with data analyzed using Combenefit software [75].

Lentiviral production and transduction, and gene depletion

HEK-293FT cells were obtained from Invitrogen (Thermo Fisher Scientific) and maintained in DMEM 10% FBS at 37°C, in a 5% CO_2 incubator and split at 70%–80% confluence. Lentiviral particles and transduction were produced following standard protocols as previously described [76], using the packing plasmid psPAX2 (Addgene, catalog 12260) and envelope plasmid pMD2.G (Addgene, catalog 12259). The MISSION®-validated short-hairpin RNA (shRNA) against human *HIF1A* expression was reported [77] (TRCN0000003810; Sigma–Aldrich) and the control vector was scrambled-pLKO.1 (Addgene, catalog 136035). The primer sequences for gene expression quantification are depicted in Supplementary Table S1.

ChIP assays

Cross-linking of proteins with DNA, fragmentation, and preparation of soluble chromatin followed by immunoprecipitation with specific antibodies were performed as previously described [78]. Briefly, 5×10^6 cells subjected or not to hypoxia, as indicated, were incubated with 1% (v/v) formaldehyde in pre-warmed PBS for 10 min at 37°C. Cells were then washed in cold PBS, harvested, and lysed to isolate nuclei in hypotonic buffer containing 5 mM PIPES at pH 8.0, 85 mM KCl, and 0.5% NP-40. Nuclei were then resuspended, lysed in a buffer containing 1% sodium dodecyl sulfate, 10 mM ethylenediaminetetraacetic acid (pH 8.0), and 50 mM Tris/HCl (pH 8.1), and sonicated in 15-ml tubes with a Bioruptor sonication device (seven cycles of 30 s ON, 30 s OFF) to yield chromatin sizes of 150–300 bp. Subsequently, 30 μg of DNA/sample was used for immunoprecipitation with 17 μl anti-MYC (N-262; Santa Cruz Biotechnology, catalog SC-764) and with the same amount of anti-rabbit IgG (Cell Signaling Technology). Immunoprecipitated and input DNAs were purified and subjected to qPCR analysis using the primers amplifying the MYC-bound regions found in *PARP1* and *POLQ* genes (Supplementary Table S1 and Text S1). Chromatin immunoprecipitation (ChIP) was quantified by real-time PCR using Roche LightCycler® 480 RT PCR. The fold enrichment of the target sequence in the immunoprecipitated (IP) relative to the input (Ref) fractions was calculated using the comparative Ct (the number of cycles required to reach a threshold concentration) method, expressed by the term $2^{-(Ct(IP)-Ct(Ref))}$.

γH2AX immunofluorescence and quantification

PC3 and T47D cells were cultured on coverslips in six-well plates and treated for 24 h with DMSO (control), rucaparib (2 μM), PX-478 (25 μM), novobiocin (100 μM), or a combination of PX-478 with either rucaparib or novobiocin. Following treatment, cells were fixed in 4% paraformaldehyde for 15 min at room temperature, permeabilized with 0.5% Triton X-100 for 15 min, and blocked in a solution of 5% normal donkey serum, 1% bovine serum albumin, and 0.01% Triton X-100 for 1 h. Cells were incubated overnight at 4°C with an anti-phospho-Ser139 γH2AX antibody (Sigma–Aldrich, catalog 05-636) diluted 1:200 in blocking solution. After primary antibody incubation, cells were washed and stained with a Cy3-conjugated donkey anti-mouse IgG secondary antibody (Jackson ImmunoResearch, catalog 715-165-151) diluted 1:400 in blocking solution containing 1 μg/ml DAPI for nuclear staining. Secondary antibody incubation was performed at room temperature for 1 h. Coverslips were mounted onto microscope slides using Fluoromount-G with DAPI (Invitrogen, catalog 00-4959-52), and images were acquired using a Zeiss LSM 980 confocal microscope. For image analysis, a custom macro was applied to quantify the integrated intensity of phospho-Ser139 γH2AX staining for individual nuclei, as defined by DAPI staining.

Deep learning tumor image modeling

We implemented the weakly supervised method of clustering-constrained-attention multiple-instance learning (CLAM) [79] for whole-slide image (WSI) processing. Feature extrac-

tion utilized the universal self-supervised model for pathology (UNI) [80], which was not trained on the histology images of TCGA. The TCGA WSIs were downloaded from the GDC Data Portal (https://portal.gdc.cancer.gov) in scanned virtual slide (SVS) format. Since SVS images contain multiple resolutions, we classified the slides based on the highest magnification level, which, for all selected cancer types, was 20× or 40×. Following the CLAM pipeline, all slides were split into patches. Specifically, the 20× images were divided into patches of 256 × 256 pixels, while the 40× images were split into 512 × 512 pixels to match the 20× resolution when downsampling. The patches were resized to 224 × 224 pixels, which was the input size for UNI, and the features of each patch were extracted into a 1024-dimensional vector. The data were split in an 80–10–10 ratio for training, testing, and validation when each predictor was represented in at least 20% of the primary tumors of a TCGA study. Otherwise, a 60–20–20 ratio was used to ensure enough positive samples for both testing and validation. We applied a dropout rate of 0.5 for training, and learning rate of 3e−5, 10-fold cross-validation, a multi-branched CLAM model type, and a limit of 10 epochs, as the models converged relatively quickly. Other parameters were left at their default settings. The same parameters were used to evaluate the algorithm's performance. All predictions based on signature scores utilized the top quartile as the threshold to distinguish between high and low tumor groups. For HRDsum scores, a cutoff of 42 was applied to both BRCA and serous ovarian (OV) tumors. However, for prostate (PRAD), where very few samples exceeded a score of 42, a cutoff of 20 was used to represent the top 25% of all samples. For generating heatmaps with attention scores, we used the same dropout rate, an overlap of 0.5, and applied a blur effect to produce smooth visual representations. The attention scores, which represent the contribution of each patch within a WSI to predict a class, were extracted for each correctly predicted sample and subsequently *Z*-score normalized. The top 20% of patches, ranked by the alt-EJ score, were selected for correlation analysis with the hypoxia and MYC scores in tumors.

Results

A cancer cell state defined by alt-EJ–TGFβ anticorrelation

HR-deficient tumors rely on alt-EJ and frequently overexpress components of this pathway [10, 35, 81–84]. To better understand the cancer cell states in which alt-EJ is active, we developed a machine-learning model to predict HR deficiency (HRD). Using the NMF method [60, 85], we identified co-regulated gene modules within the TCGA BRCA dataset [37, 61], resulting in 24 gene modules (Fig. 1A). These modules were used to predict HRD based on the HRDsum score, a genomic metric quantifying HRD in cancer cells by integrating measures of loss of heterozygosity, telomeric allelic imbalance, and chromosomal state transitions [39]. The model demonstrated high predictive accuracy, achieving Spearman correlation coefficients of 0.90 and 0.81 between predicted and observed HRDsum scores in the training and test subsets, respectively (Fig. 1B).

To understand the contribution of each gene module to HRD status, we calculated average SHAP values, which quantify the contribution of each module to the prediction. This analysis revealed that module 2 had the strongest positive association with HRDsum, while module 11 exhibited the strongest negative association (Fig. 1C). Consistent with these findings, the gene expression signature associated with alt-EJ activity [33, 35, 36] was positively correlated with module 2 and negatively correlated with module 11 (Fig. 1D, left panels). In contrast, the signature of TGFβ signaling activity [33, 35, 36] was positively correlated with both modules (Fig. 1D, right panels). The positive correlation of TGFβ signaling activity with both modules suggests its pleiotropic function and/or an indirect role in the transcriptional regulation of alt-EJ, independent of small mothers against decapentaplegic (SMAD) factors. Prior studies have shown that BRCA1 loss promotes luminal-to-basal transformation and EMT in breast cancer [86–88], a process mediated by TGFβ receptor 2 [89].

Since module 11 exhibited the strongest negative association with HRDsum, we performed additional analyses to examine its associations with curated gene sets representing various health and disease states [67]. In addition to EMT, this module showed positive associations with stemness-related pathways, including Hedgehog, NOTCH, and WNT/β-catenin signaling, as well as hypoxia signaling (Fig. 1E and Supplementary Table S2). Conversely, it displayed negative associations with gene sets related to E2F and MYC targets (Fig. 1E), suggesting a potential link to cell cycle regulation [90, 91].

Hypoxia signaling is anticorrelated with alt-EJ

TGFβ signaling is known to promote the expression and stabilization of HIF1α (encoded by the *HIF1A* gene) [92–95]. Consistently, the alt-EJ signature was found to be negatively correlated with both *HIF1A* expression and a 15-gene hypoxia signature [56] across most cancer types analyzed ($n = 25$; Fig. 2A). At the single-cell level, transcriptional analysis of four cancer cell lines exposed to TGFβ-1 [42] revealed progressive upregulation of both the TGFβ and hypoxia signatures, along with downregulation of the alt-EJ signature (Fig. 2B), supporting the pan-cancer observation.

We then explored the relationship between alt-EJ and TGFβ signatures in TCGA KIRC stratified by the status of the von Hippel–Lindau (VHL) tumor suppressor, which targets HIF1α for proteasomal degradation [96]. While the overall KIRC dataset did not show a significant anticorrelation between alt-EJ and TGFβ [$n = 534$; Pearson's correlation coefficient (PCC) $= -0.08$; $P = .078$], a significant anticorrelation was observed in *VHL*-mutant tumors ($n = 173$; PCC $= -0.18$; $P = .012$; Fig. 2C). Next, we compared the alt-EJ signature between tumors with frameshift, missense, or nonsense mutations in *HIF1A* and those without mutations. Although *HIF1A* mutations are relatively rare, a substantial number of predicted deleterious variants are identified in TCGA by the OncoKB mutation database [41, 97] in cBioPortal [38] (Supplementary Table S3). The uterine corpus endometrial carcinoma (UCEC) dataset had the largest number of *HIF1A* mutations ($n = 25$), with mutated tumors showing significant overexpression of the alt-EJ signature (Fig. 2D). This pattern was also observed across all examined TCGA cancer types, where tumors harboring *HIF1A* mutations ($n = 76$) exhibited significantly higher alt-EJ signature expression (Fig. 2E). To further investigate the role of HIF1α in alt-EJ suppression, we analyzed transcriptomic data from HCT116 colorectal cancer cells comparing *HIF1A*-deleted ($HIF1A^{-/-}$) to WT ($HIF1A^{+/+}$) cells under normoxic or hypoxic (1% O_2

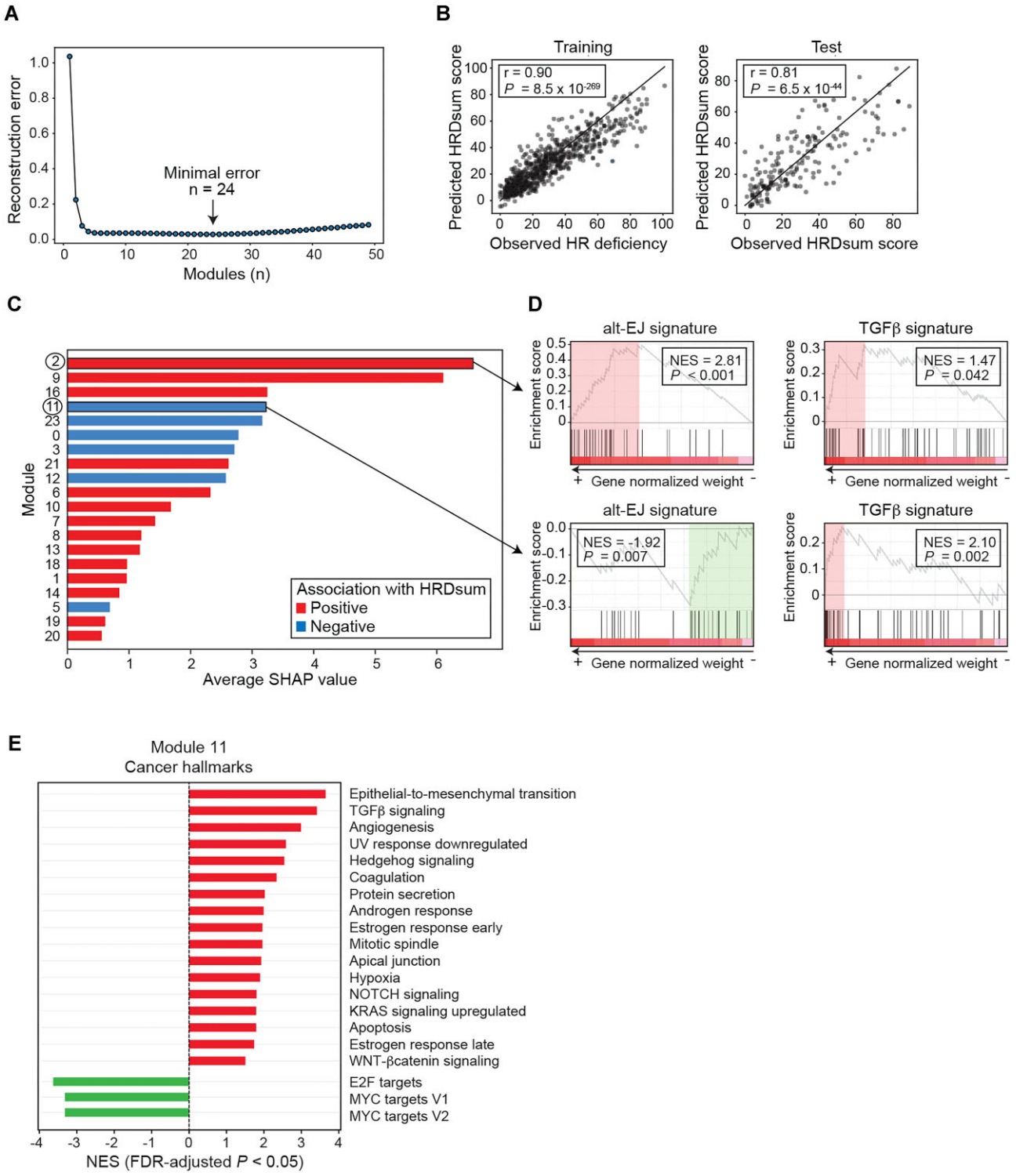

Figure 1. Cancer gene modules associated with HR status. (**A**) Graph showing the reconstruction error of the original TCGA BRCA tumor-by-gene matrix using consecutive sets (*n*) of NMF modules. The set with minimum error is indicated. (**B**) Scatter plots showing the Spearman correlation coefficient (*r*) and associated *P* between the predicted and observed HR-deficiency score (HRDsum) using the machine learning model. Left and right panels show the results of the training and test sets, respectively. (**C**) Average SHAP values of NMF gene modules, with modules 2 and 11 (highlighted with circles) showing the strongest positive and negative contributions to HRDsum prediction, respectively. (**D**) GSEA outputs of the alt-EJ (left panel) and TGFβ (right panel) signatures in modules 2 (top panel) and 11 (bottom panel). The GSEA normalized enrichment scores (NESs) and statistical significance (*P*) are indicated. (**E**) Histogram depicting the GSEA "Cancer Hallmarks" gene sets positively [false-discovery rate (FDR)-adjusted $P < .05$; NESs > 1.0; red bars] and negatively (FDR-adjusted $P < .05$; NESs < 1.0; green bars) associated with module 11. The MYC V1 and V2 gene sets correspond to curated MYC target sets from The Molecular Signatures Database.

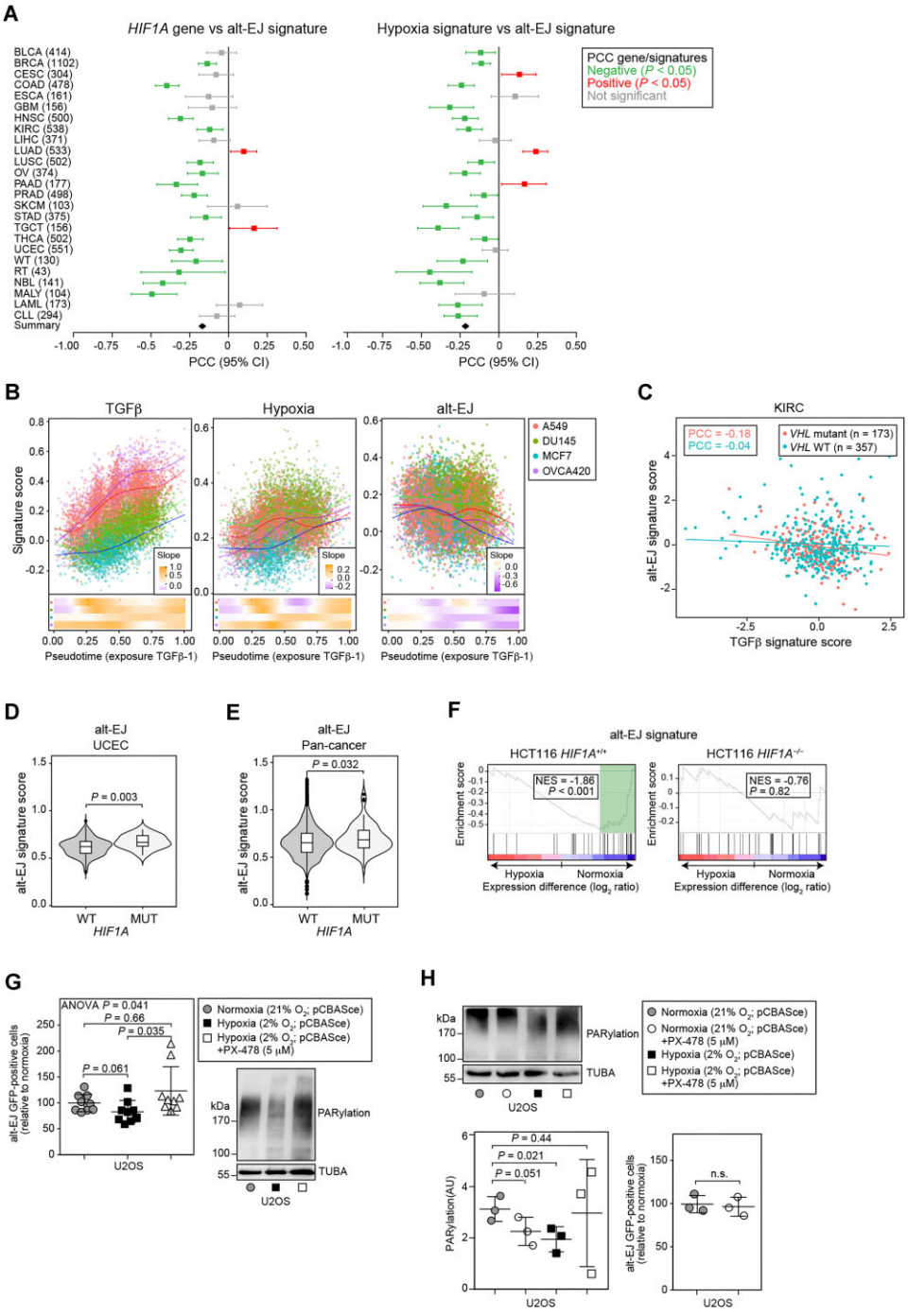

Figure 2. Hypoxia signaling anticorrelates with alt-EJ. (**A**) Forest plots showing the correlation (PCC and 95% CI) between the alt-EJ signature and *HIF1A* or the hypoxia 15-gene signature across various cancer types (study acronyms and tumor frequencies are displayed). Nominally significant correlations ($P < .5$) are indicated in the inset. (**B**) Plots of the TGFβ (left panel), hypoxia (middle panel), and alt-EJ (right panel) signature scores over time (pseudotime) in single cancer cells (A549, lung; DU145, prostate; MCF7, breast; and OVCA420, ovarian) exposed to TGFβ-1. The slopes from the numerical differentiation of the signatures are shown at the bottom. (**C**) Scatter plot showing the alt-EJ–TGFβ correlation (PCC) in TCGA KIRC tumors stratified by *VHL* status, as indicated in the inset. (**D**) Violin plot showing the overexpression of the alt-EJ signature in *HIF1A* mutated (MUT) relative to WT TCGA UCEC tumors. The significance (*P*) of the two-tailed Mann–Whitney test is indicated. (**E**) Violin plot showing the overexpression of the alt-EJ signature in *HIF1A* mutated (MUT) relative to WT TCGA pan-cancer ($n = 19$ cancer types). The significance (*P*) of the two-tailed Mann–Whitney test is indicated. (**F**) GSEA outputs of the alt-EJ signature in HCT116 *HIF1A* WT (left panel) and *HIF1A*-deteled (right panel) cells exposed to hypoxia versus normoxia. The GSEA–NESs and *P*-values are indicated. (**G**) Left panel, normalized activity of alt-EJ as measured by the EJ2-GFP reporter in UOS cells grown in hypoxia relative to hypoxia and exposed to PX-478, as indicated in the inset ($n = 4$ independent assays). The significance (*P*) of the one-way ANOVA test with Tukey correction is indicated. There are also indicated the *P*-values of the two-tailed Student's paired-samples *t*-test. Right bottom panel, representative western blot results of PARylation in the above conditions. (**H**) Top-left panel, representative western blot results of PARylation in the following four UOS cell assays: normoxia; normoxia plus exposure to PX-478; hypoxia; and hypoxia plus exposure to PX-478, as indicated in the inset. Bottom left panel, quantification of PARylation relative to loading control in three independent assays. The significance of the two-tailed Student's paired-samples *t*-test relative to normoxia is indicated. Bottom right panel, quantification of alt-EJ as measured by the EJ2-GFP reporter in UOS cells grown in normoxia relative to normoxia and exposed to PX-478.

for 90 min) conditions [43]. WT cells showed suppression of alt-EJ under hypoxia, while this effect was absent in *HIF1A*-deleted cells (Fig. 2F).

To assess the impact of hypoxia on alt-EJ pathway activity, we used human osteosarcoma U2OS cells with a GFP-based reporter for alt-EJ repair [72] and measured PARylation in cell extracts [98]. PARylation, also known as polyADP-ribosylation—the addition of ADP-ribose molecules to target proteins—is essential for DNA repair and serves as a functional indicator of alt-EJ repair [99–101]. Cells cultured under hypoxia (2% O_2 for 24 h) exhibited a trend toward reduced alt-EJ repair compared with normoxia, with an average suppression of 19% (unpaired two-tailed Student's *t*-test, $P = .061$; $n = 4$ independent assays; n = 2–3 replicates/assay; Fig. 2G). Treatment with PX-478 (5 μM), an inhibitor of both constitutive and hypoxia-induced HIF1α expression [102–105], restored alt-EJ repair to an average level similar to normoxia, though outliers were noted (Fig. 2G). At the molecular level, hypoxia reduced PARylation, which appeared to be restored by PX-478 treatment (Fig. 2G). To further assess this observation, we quantified PARylation in three additional assays under the same conditions and including cells treated with PX-478 (5 μM) in normoxia. A significant reduction in PARylation was only observed in cells grown under hypoxia compared with those in normoxia (Fig. 2H).

Interplay between hypoxia and MYC influences alt-EJ

Machine-learning modeling predicted that MYC promotes alt-EJ gene expression in TCGA BRCA, as shown by negative GSEA–NES associations (green bars in Fig. 1E). A positive correlation between *MYC* and alt-EJ expression was observed in 11 of 25 (44%) cancer types analyzed (Fig. 3A, left panel). When a MYC-driven gene signature [58] was analyzed, this positive association was confirmed across all cancer types (Fig. 3A, right panel). Supporting this, 83% (30/36) of the genes in the alt-EJ signature were predicted to be MYC targets based on ChIP data from the ChIP-Atlas [106], and promoter sequences of alt-EJ genes were significantly enriched for MYC binding across various cell types (Fig. 3B).

To experimentally assess the influence of TGFβ/hypoxia on alt-EJ, we used MCF10A epithelial cells, which can undergo EMT and acquire stemness upon exposure to TGFβ-1 or hypoxia [107–109]. Transcriptomic analysis of MCF10A cells exposed to TGFβ-1 (500 pg/ml for 6 h) [69] revealed upregulation of the TGFβ and hypoxia signatures, along with downregulation of the alt-EJ and MYC signatures (Fig. 3C). Semi-quantitative gene expression analysis in MCF10A cells under hypoxia (2% O_2 for 8 h) showed significant downregulation of *PARP1* and *POLQ* by approximately 30%, while hypoxia-induced genes exhibited the expected opposite trend (Fig. 3D). Analogous TaqMan-based assays showed similar downregulation of *PARP1* and *POLQ* in hypoxia, though statistical significance was limited to *POLQ* suppression (Fig. 3E). In agreement with prior studies demonstrating hypoxia-induced suppression of HR and NHEJ components [110, 111], *BRCA1*, *PRKDC*, and *RAD51* were also downregulated (Fig. 3E, middle panel). Further analysis of MCF10A cells treated with the hypoxia mimetic $CoCl_2$ (200 μM for 24 h) showed significant reductions in *PARP1* (25%) and *POLQ* (70%) expression (Fig. 3F). In addition, assessing the association between the hypoxia signature and PARP1 protein expression measured by mass spectrometry in hundreds of cancer cell lines (CCLE and GDSC datasets [50, 51]; POLθ was not reported) showed significant anticorrelation (Fig. 3G). Akin to these suppressions, ChIP assays demonstrated hypoxia-induced reductions in MYC binding at the *PARP1* and *POLQ* promoters in MCF10A cells grown under hypoxia (2% O_2 for 8 h) compared with normoxia (Fig. 3H).

The opposing roles of hypoxia and MYC in regulating alt-EJ were further assessed using multivariate regression analyses of the alt-EJ/TGFβ ratio across TCGA studies, accounting for cell cycle signatures [68] or *MKI67* expression. Hypoxia and MYC signatures were negatively and positively associated, respectively, with the alt-EJ/TGFβ ratio ($\beta \leq -0.13$; $P = 4 \times 10^{-13}$ and $\beta \geq 0.38$; $P < 2 \times 10^{-16}$; Supplementary Tables S4 and S5). A significant interaction between hypoxia and MYC signatures ($P_{interaction} = .02$) further supported their opposing roles, as confirmed by analysis across tertiles of the alt-EJ/TGFβ ratio (Fig. 3I). Incorporating the HRDsum score into the regression analysis showed that the effects of hypoxia (negative) and MYC (positive) on alt-EJ were independent of HR status (Supplementary Tables S6 and S7). Similarly, correlations between alt-EJ and hypoxia/TGFβ (negative) or MYC (positive) signatures were consistent in TCGA BRCA and TCGA OV tumors, regardless of HRD or HR proficiency as defined by HRDsum (Supplementary Fig. S1). These findings highlight that hypoxia/TGFβ and MYC exert opposing effects on alt-EJ gene expression, independent of HR status.

Combined inhibition of HIF1α and PARP or polθ synergistically reduces CFC

Given that hypoxia signaling is often abnormally activated in cancer [112], we hypothesized that targeting this pathway could relieve suppression of alt-EJ and increase sensitivity to PARP or POLθ inhibitors. To test this, we analyzed the basal signature scores from hundreds of cancer cell lines and their response to PARPi (CCLE dataset [44]). Unsupervised clustering of the alt-EJ, hypoxia, MYC, and TGFβ signatures revealed two major clusters (A and B; Supplementary Fig. S2A). Cluster B, characterized by high alt-EJ and MYC signature expression, and low hypoxia and TGFβ signature expression, showed greater sensitivity (i.e. lower IC_{50}) to PARPi (Supplementary Fig. S2B, C). Similar patterns were observed with three-cell clusters (Supplementary Fig. S2D).

We then performed CFC assays on HR-proficient human breast (MDA-MB-231, T47D) and ovarian (A2780, OVCAR4) cancer cell lines, as well as HR-proficient (DU145, PC3) and HR-deficient (22Rv1, *BRCA2*-mutant) prostate cancer cell lines, exposed to compound or drug inhibition of HIF1α and/or PARP or POLθ. For these assays, we used PX-478, PARP inhibitors (olaparib, rucaparib, and talazoparib), or the POLθ inhibitor novobiocin [24]. In two-dimensional viability assays, the IC_{50} values of these drugs were frequently ≥10 μM, consistent with large screening datasets [45, 113] (Supplementary Tables S8 and S9). Cancer cells frequently exhibit some degree of HIF1α activation, even in normoxic conditions [114]. Consistently, the hypoxia signature scores of the selected cell lines (except of DU145, which lacked CCLE gene expression data) grown under normoxia were, on average, intermediate between the scores of cancer cell lines with deleterious *HIF1A* and *VHL* variants (Supplementary Fig. S3).

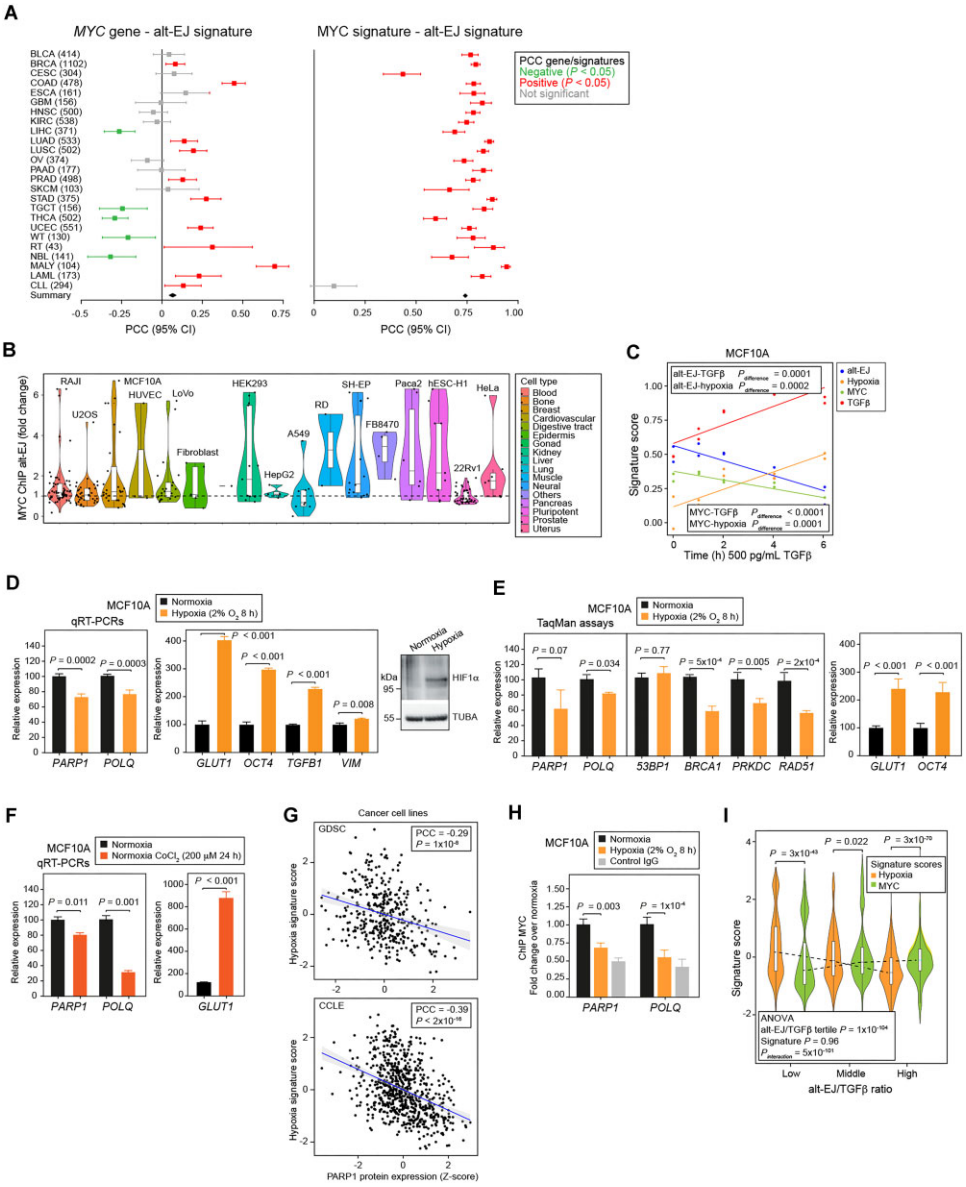

Figure 3. Interplay between hypoxia and MYC regulates alt-EJ. (**A**) Forest plots showing the correlation (PCC and 95% CI) between the alt-EJ signature and MYC expression (left panel) or the MYC-driven signature (right panel) across various cancer types (study acronyms and tumor frequencies are indicated). Nominally significant correlations ($P < .05$) are indicated in the inset. (**B**) Violin plot showing MYC-binding (fold change) at the promoter regions (±5 kb from transcription start site) of alt-EJ genes, across tissue (inset). The results correspond to the tissue with ≥1 cell line (dots) with a significant MYC-binding at the alt-EJ promoter set (FDR-adjusted Fisher's exact test $P < .05$). The cell lines with the highest MYC-binding in each tissue type are indicated. (**C**) Graph showing the time-course trends of the expression of the alt-EJ, hypoxia, MYC, and TGFβ signatures in MCF10A cells exposed to TGFβ-1 (500 pg/ml) for 0 to 6 h. The significance (*P*) of the difference in the hypoxia and TGFβ signature slopes relative to alt-EJ (top inset) and MYC (bottom inset) signature slopes are indicated. (**D**) Left panel, downregulation of *PARP1* and *POLQ1* (quantitative reverse transcription polymerase chain reaction (qRT-PCR) assays with specific primers and SYBR) in MCF10A cells cultured in hypoxia, as indicated in the inset. The bars show the mean ± standard deviation (s.d.), and the two-tailed Student's unpaired-samples *t*-test *P*-values are indicated ($n = 3$ independent assays; 3 replicates/assay). Middle panel, overexpression of *GLUT1*, *OCT4*, *TGFβ1*, and *VIM* in MCF10A cells cultured in hypoxia, as indicated in the inset. Right panel, western blot showing overexpression of HIF1α in MCF10A cells under hypoxia. The loading control, α-tubulin (TUBA), is also shown. (**E**) Left panel, downregulation of *PARP1* and *POLQ1* (TaqMan assays) in MCF10A cells cultured under hypoxia, as indicated in the inset. The bars show the mean ± s.d., and the two-tailed Student's unpaired-samples *t*-test *P*-values are indicated ($n = 2$ independent assays; 4 replicates/assay). Middle panel, results for genes involved in HR or NHEJ pathways. Right panel, confirmation of overexpression of *GLUT1* and *OCT4* in the cells under hypoxia. (**F**) Left panel, downregulation of *PARP1* and *POLQ1* (qRT-PCR assays with specific primers and SYBR) in MCF10A cells cultured in normoxia and exposed to $CoCl_2$, as indicated in the inset. The bars show the mean ± s.d., and the two-tailed Student's unpaired-samples *t*-test *P*-values are indicated. Right panel, confirmation of *GLUT1* overexpression in the cells exposed to $CoCl_2$. (**G**) Anticorrelation between the hypoxia signature and PARP1 protein expression in the GDSC and CCLE datasets. The correlation (PCC) and corresponding significance (*P*) are indicated. (**H**) Reduced MYC binding at the promoters of the *PARP1* and *POLQ* genes in MCF10A cells grown under hypoxia, as indicated in the inset. The results are shown as the MYC-binding fold change relative to normoxia, including control isotype immunoglobulin (IgG). The unpaired two-sided Student's *t*-test *P*-values are indicated ($n = 2$ independent assays; 3 replicates/assay). (**I**) Violin plot showing the distributions of the alt-EJ and hypoxia signature scores (inset) in the tertiles of the ratio of the alt-EJ/TGFβ signature scores in TCGA cancer types ($n = 19$). Trends in the alt-EJ and hypoxia signature are denoted by dashed lines. The paired two-sided Student's *t*-test *P*-values are indicated for the signature comparisons in each tertile of the alt-EJ/TGFβ ratio. Significance (*P*) of the ANOVA of the alt-EJ/TGFβ ratio and signature score terms and their interaction are also indicated (bottom inset).

The combination of PX-478 (5 μM; IC_{50} values between 10 and 42 μM) with rucaparib (PARPi, 2 μM; IC_{50} values between 20 and 302 μM) showed evidence of synergy (Bliss [73] scores ≥ 16) in five cell lines (excluding A2780 and 22Rv1; $n = 2$ independent assays; $n = 3$ replicates/assay; Fig. 4A). In parallel, dose-response matrices over 72 h showed synergistic effects in six cell lines (excluding OVCAR4; Fig. 4B). The synergy was also assessed by combining PX-478 (5 μM) with two other PARP inhibitors (olaparib, 2 μM, and talazoparib, 1 nM) in three cell lines (OVCAR4, PC3, and T47D). These CFC assays yielded Bliss synergy scores ≥ 14 in 6/7 of the settings ($n = 2$ independent assays; $n = 3$ replicates/assay; Supplementary Fig. S4). Synergistic effects were also observed in high-confluence settings across all cell lines tested (Supplementary Fig. S5).

The molecular alterations underlying the synergy between HIF1α and PARPi were assessed in DU145 cells. PX-478 25 μM (DU145 $IC_{50} = 27.5$ μM) for 24 h reduced HIF1α expression and increased PARylation, while the combination with rucaparib strongly suppressed both HIF1α and PARylation (Fig. 4C). An analogous assay substituting rucaparib with olaparib showed similar changes in PARylation and HIF1α levels (Fig. 4D). In addition, DU145 cells exposed to hypoxia (2% O_2 for 8 h) showed a significant decrease in PARylation (Fig. 4E). Furthermore, similar to MCF10A cells, MYC binding at the promoters of *PARP1* and *POLQ* was significantly reduced in DU145 cells grown under hypoxia (2% O_2 for 8 h) compared with those grown under normoxia (Fig. 4F). To determine whether the observed alteration in MYC binding was influenced by changes in *MYC* expression, we analyzed *MYC* expression in the seven cell lines under normoxic and hypoxic conditions. This analysis did not reveal a consistent alteration in *MYC* expression levels (Supplementary Fig. S6A). Furthermore, the expression of *MYC* and its gene product showed no clear correlation with the hypoxia signature score in the CCLE dataset (Supplementary Fig. S6B).

Next, similar CFC assays were performed using the POLθ inhibitor novobiocin [24]. This drug was applied at a concentration of 100 μM, selected based on its reported high IC_{50} values and minimal effect on HR-proficient cells [24, 115–119] (IC_{50} values > 269 μM in the seven cell lines analyzed; Supplementary Table S9). The combination of PX-478 (5 μM) with novobiocin showed synergistic effects (Bliss synergy scores ≥ 12) in 4/7 of the cell lines ($n = 2$ independent assays; $n = 3$ replicates/assay Fig. 5A). The combination of novobiocin or rucaparib with PX-478 was also assessed using acriflavine, which reduces HIF1α signaling [120, 121]. Bliss synergy scores ≥ 14 indicated synergism in 67% (4/6) of the tests conducted in three cell lines at relative high confluence (OVCAR4, PC3, and T47D; $n = 3$ independent assays; $n = 3$ replicates/assay; Supplementary Fig. S7A). In these assays, exposure to acriflavine increased PARylation while rucaparib reduced this activity (Supplementary Fig. S7B).

To test the prediction that combined inhibition of HIF1α and PARP or POLθ leads to increased DNA damage, we measured phospho-Ser139 γH2AX levels in PC3 and T47D cells. Cells were treated with DMSO, rucaparib (2 μM), PX-478 (25 μM), novobiocin (100 μM), or combinations of rucaparib and PX-478, as well as novobiocin and PX-478, for 24 h. PX-478 treatment alone caused a substantial increase in phospho-Ser139 γH2AX (Fig. 5B), consistent with prior findings [122]. Compared with PX-478 alone, the combination with rucaparib led to a slight, nonsignificant increase in γH2AX signal; however, the combination with novobiocin resulted in a significantly greater increase in phospho-Ser139 γH2AX in both cell lines (Fig. 5B). The underlying basis of these differential effects is unclear but may reflect the distinct roles of PARP1 and POLθ in DSB repair and alt-EJ/MMEJ, and the evaluation of HR-proficient backgrounds.

To assess the effect of targeting *HIF1A*, we performed CFC assays using a shRNA directed against its expression (shHIF1A) [77] or a scrambled shRNA as a negative control. The combination of shHIF1A with rucaparib (2 μM) or novobiocin (100 μM) showed a stronger inhibitory effect (unpaired two-tailed t-test $P < .05$) than the single-target assays in the three cell lines analyzed, with evidence of synergy in 50% (3/6) of the assays (Bliss synergy scores ≥ 13; Fig. 5C and Supplementary Fig. S8). However, transduction with shHIF1A alone caused strong inhibition across the three cell lines and, unexpectedly, frequently reduced PARylation and *PARP1* expression relative to pLKO (Supplementary Fig. S9). These findings indicate that targeting *HIF1A* expression may induce additional molecular alterations that influence cell viability and drug combination effects.

Deep-learning prediction of alt-EJ and hypoxia in tumor pathology images for precision cancer treatment

The observed influence of HIF1α on alt-EJ offers potential for improving predictions of targeted therapy outcomes. To explore this, we analyzed spatial transcriptomics data from a GBM dataset [55]. Among the tumors in this study with informative expression of both alt-EJ and hypoxia signatures, 63% (5/8) showed a significant negative correlation between these signatures (PCC ≤ −0.10; $P < 1 \times 10^{-8}$), while only one tumor exhibited a positive alt-EJ–hypoxia correlation (PCC = 0.12; Fig. 6A).

Next, we applied a deep-learning method [79, 80] to predict alt-EJ and hypoxia status, as well as common gene drivers, using tumor pathology images from TCGA BRCA [61], OV [123], and PRAD [124] cancers. The method demonstrated strong performance for both signatures, with area under the receiver operating characteristic curve (AUCROC) values of ≥0.70 in all settings. The AUCROC for alt-EJ was 0.768 ± 0.059, 0.702 ± 0.086, and 0.830 ± 0.0638, and for hypoxia, the AUCROC was 0.732 ± 0.051, 0.719 ± 0.044, and 0.621 ± 0.070 for BRCA, OV, and PRAD, respectively (Supplementary Table S10 and Fig. S10A). The method also performed relatively well in predicting MYC signature activity, with an AUCROC of 0.859 ± 0.058, 0.698 ± 0.064, and 0.821 ± 0.069 for BRCA, OV, and PRAD, respectively (Supplementary Fig. S10B). Among other features analyzed, the best performance were achieved in predicting *TP53* mutation and tumor subtype (PAM50 [61]) in BRCA: AUCROC of 0.828 ± 0.068 and 0.892 ± 0.022, respectively (Supplementary Fig. S10C and D).

The analysis of the spatial distribution of inferred alt-EJ activity and hypoxia signaling in tumor images further emphasized their anticorrelation. This relationship was particularly evident in a basal-like breast tumor from a patient with a germline pathogenic *BRCA1* variant. While the tumor was predicted to have high levels of both alt-EJ and hypoxia, the attention scores—indicating the model's focus on specific tumor regions during signature prediction—showed an inverse pattern across tumor patches (Fig. 6B). To further investigate

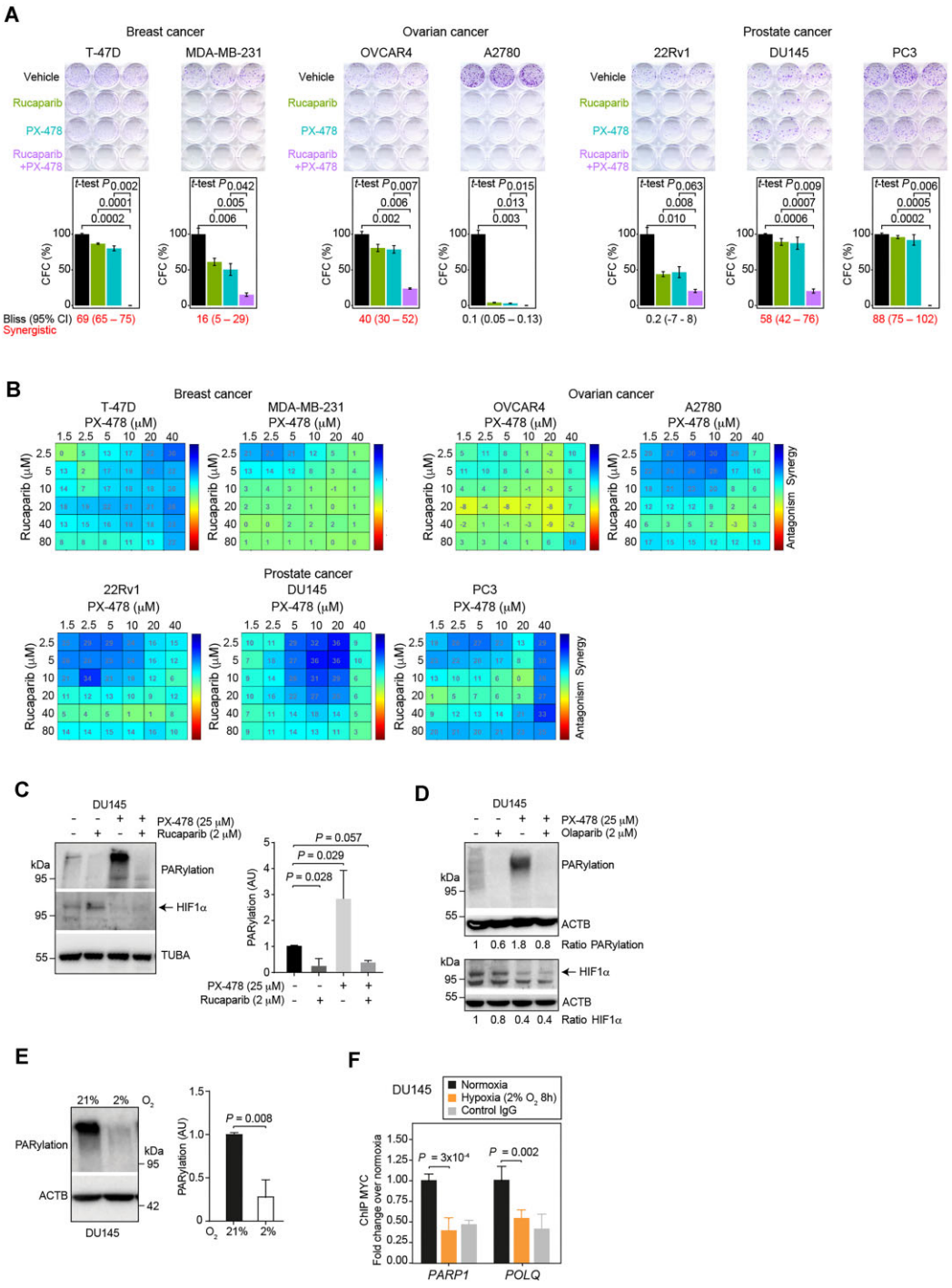

Figure 4. Synergy between HIF1α and PARPi in reducing cancer cell CFC. (**A**) Results of CFC assays in breast, ovarian, and prostate cancer cell lines exposed to vehicle (DMSO), rucaparib (2 μM), PX-478 (5 μM), and the combination of rucaparib and PX-478. The graphs show the mean ± s.d. The unpaired two-sided Student's *t*-test *P*-values for the comparisons with the drug combination group are indicated. The Bliss synergy score (95% CI) is indicated at the bottom of each panel (Bliss score > 10 indicates synergism). (**B**) Drug dose matrix of PX-478 and rucaparib in cell viability assays. The color scale indicates synergy or antagonism, with the numbers in the cells denoting the percent difference in loss of viability compared with expected values assuming no synergy. (**C**) Left panel, western blot results of PARylation and HIF1α levels in DU145 cells exposed for 24 h to vehicle (DMSO), rucaparib (2 μM), PX-478 (25 μM), or the combination of the two drugs. The molecular weights, in kDa, are indicated. The results of the loading control (TUBA) are also shown. Right panel, quantification (arbitrary units, AU) of PARylation under previous conditions. The significance (*P*) of the two-tailed Mann–Whitney test is indicated (mean ± s.d.; $n = 4$ independent assays). (**D**) Western blot analysis of PARylation and HIF1α levels in DU145 cells exposed for 24 h to vehicle (DMSO), olaparib (2 μM), and/or PX-478 (25 μM). PARylation and HIF1α levels are denoted in each condition as the ratio of the corresponding signal to the loading control (β-actin, ACTB), normalized to the basal condition without drug treatment (set as 1). (**E**) Left panel, western blot results of total PARylation in DU145 cells grown under normoxia or hypoxia. The results of the loading control (ACTB) are also shown. Right panel, quantification (AU) of PARylation under previous conditions. The significance (*P*) of the two-tailed Mann–Whitney test is indicated (mean ± s.d.; $n = 5$ independent assays). (**F**) Graph showing the ChIP assays of MYC binding at the promoters of the *PARP1* and *POLQ* genes in DU145 cells grown under normoxic or hypoxic conditions, as indicated in the inset. The results are shown as MYC-binding fold change relative to normoxia, including the control IgG. The unpaired two-sided Student's *t*-test *P*-values are indicated ($n = 2$ independent assays; 3 replicates/assay).

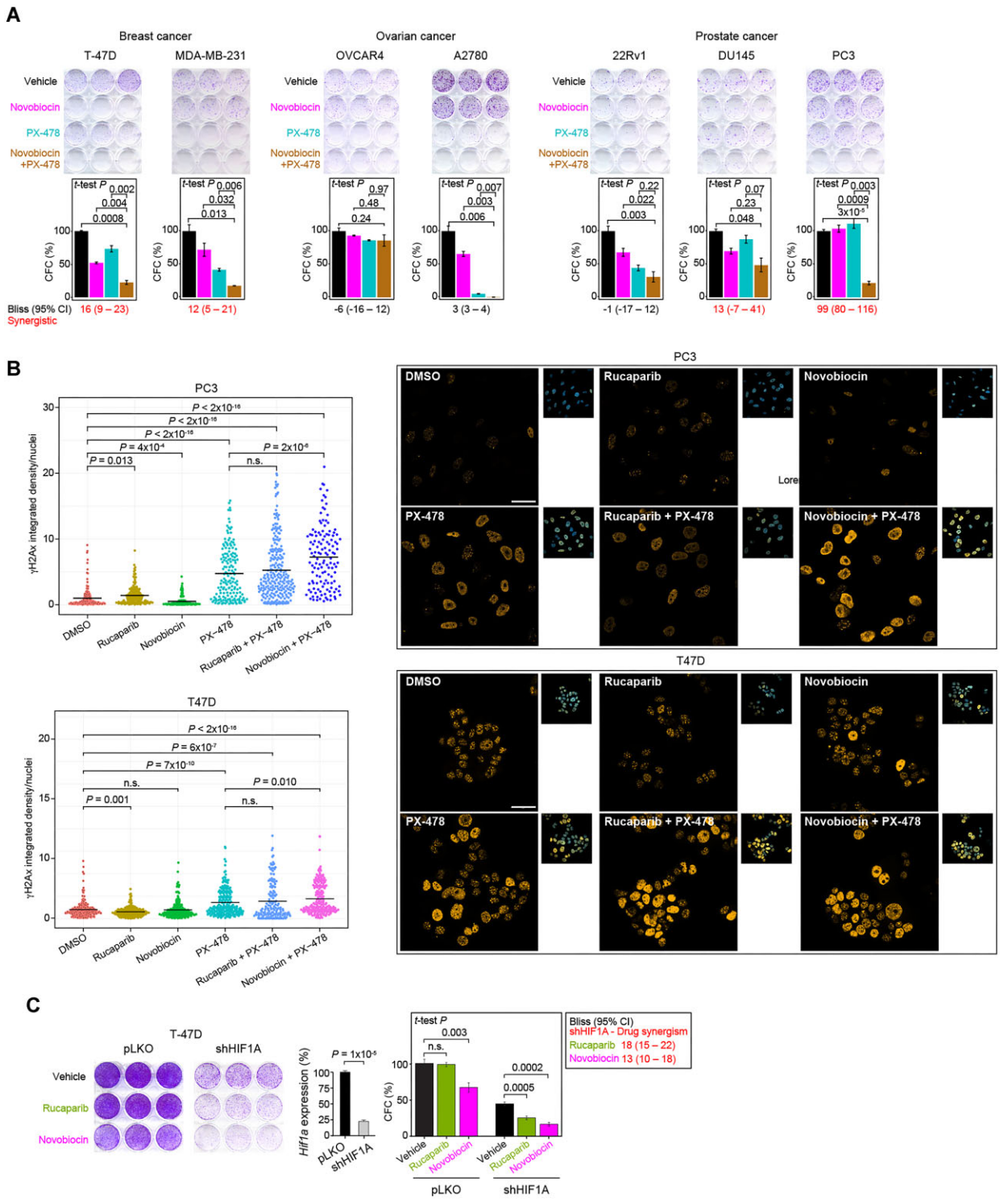

Figure 5. Synergy between HIF1α inhibition or *HIF1A* expression depletion and POLθ or PARPi in reducing cancer cell CFC. (**A**) CFC assays for vehicle (DMSO), novobiocin (100 μM), PX-478 (5 μM), and the combination of novobiocin and PX-478. The graphs indicate mean ± s.d. The unpaired two-sided Student's *t*-test *P*-values for the comparisons with the drug combination group are indicated. The Bliss synergy score (95% CI) is indicated at the bottom of each panel (Bliss score > 10 indicates synergism). (**B**) Left panels, graphs showing the integrated density of phospho-Ser139 γH2AX signal per nucleus: top, PC3 cells; bottom, T47D cells. Data are presented as ≥ 100 nuclei per condition, with the mean value indicated by a horizontal line. The significance of the one-way ANOVA test is shown for all conditions relative to DMSO and for drug combinations relative to PX-478 alone. Right panels, representative images of phospho-Ser139 γH2AX immunodetection under the same conditions. The smaller images show the 4′,6-diamidino-2-phenylindole (DAPI) merge for nuclear staining. (**C**) Left panels, CFC assays for vehicle (DMSO), rucaparib (2 μM), and novobiocin (100 μM) in T47D cells transduced with pLKO or shHIF1A. Middle panel, semi-quantitative gene expression analysis of *HIF1A* in the assayed T47D cells; the graphs show the mean ± s.d. ($n = 2$ independent assays; 3 replicates/assay) relative to pLKO, and the *PPIA* gene was used as the control. The unpaired two-sided Student's *t*-test *P*-value is indicated. Right panel, the graph shows the mean ± s.d. The unpaired two-sided Student's *t*-test *P*-values for the comparisons with the vehicle are indicated. The Bliss synergy score (95% CI) is indicated at the bottom of each panel (Bliss score > 10 indicates synergism).

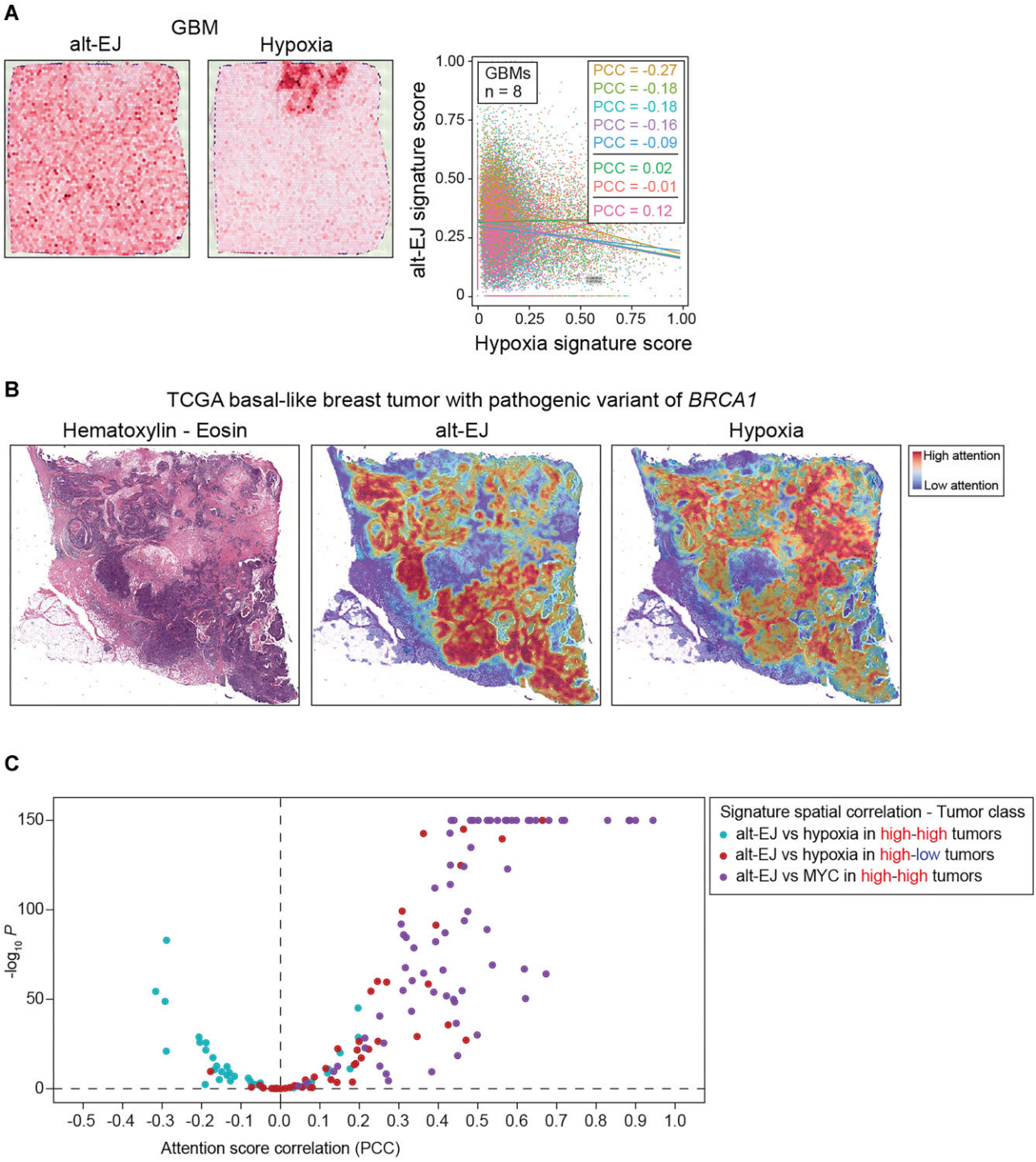

Figure 6. Deep learning classification of alt-EJ and hypoxia status. (**A**) Left panels, representative images of the inferred alt-EJ and hypoxia signature scores in a GBM tissue. Right panel, scatter plot of the alt-EJ–hypoxia signature (standardized score) correlation in GBM tumors ($n = 8$). The corresponding PCCs are shown: five are significantly ($P < .05$) negative, two are not significant, and one is significantly positive. (**B**) Pathology image, and alt-EJ and hypoxia attention maps of a TCGA basal-like (PAM50-classified) breast tumor developed in a women carrier of a *BRCA1* pathological variant (tumor ID: TCGA-AN-A0XU). (**C**) Volcano plot for PCCs between the alt-EJ and hypoxia or MYC signature attention scores in breast tumors correctly classified as "high-alt-EJ and high-hypoxia", "high-alt-EJ and low-hypoxia", or "high-alt-EJ and high-MYC", as indicated in the inset. The tumors with "high-alt-EJ and high-hypoxia" tended to show alt-EJ-hypoxia anticorrelation.

this observation, we examined the correlation between the signature attention scores in breast tumors correctly categorized as either "high-alt-EJ and high-hypoxia" (high–high; n = 37) or "high-alt-EJ and low-hypoxia" (high–low; $n = 44$). Consistent with the HIF1α-mediated suppression of alt-EJ, tumors in the high–high category frequently showed anticorrelations between alt-EJ and hypoxia scores, whereas positive correlations were common in the high–low category (Fig. 6C). Additionally, we observed that alt-EJ and MYC scores were positively correlated in most tumors (Fig. 6C). The molecular insights gained from this study, combined with the deep-learning approach, have the potential to improve patient stratification for precision treatment and guide future research on synergistic drug combinations.

Discussion

Based on gene expression, molecular, and cellular assays conducted across various cancer models and conditions, our study demonstrates that HIF1α suppresses alt-EJ gene expression and pathway function. Consequently, depletion or inhibition of HIF1α enhances alt-EJ activity, revealing a mechanism by which sensitivity to PARP and POLθ inhibitors can be increased in cancer cells, regardless of HR status. Incorporating these findings with the ability to predict alt-EJ and HIF1α competency using tumor pathology images could improve patient stratification and enhance therapeutic outcomes with PARPi and POLθi. Our pan-cancer observations and mechanistic insights build on the association between resistance to neoadjuvant talazoparib in *BRCA1*-mutant breast cancer and the basal expression of hypoxia and stem cell-related signatures [125]. Furthermore, our evidence aligns with recent findings that EMT, stemness, and hypoxia-related transcriptional programs contribute to cancer cell adaptation to PARPi [126]. Collectively, our data provide a rationale for future clinical trials combining PARPi or POLθi with HIF1α-targeting compounds [127, 128], which are predicted to synergistically enhance efficacy even in cancers with functional HR-mediated DNA repair.

The opposing effects of HIF1α and MYC on the transcriptional regulation of alt-EJ reveal a functional interaction between these master regulators that may influence cancer cell states and vulnerabilities. HIF1α and MYC generally have contrasting roles in regulating cell cycle progression and proliferation in cancer cells [129–131]. HIF1α promotes cell cycle arrest by partially displacing MYC from the promoters of cell cycle inhibitor genes [132]. By restricting proliferation, HIF1α also competes with MYC for the promoters of genes involved in HR- and mismatch-mediated DNA damage repair [110, 133]. HIF1α further represses HR-associated genes through additional mechanisms [111]. However, complete cell cycle arrest is expected only under severe hypoxic conditions (approximately <0.1% O_2). Most cancer cells within a tumor reside in microenvironments of moderate or mild hypoxia, typically between 0.5% and 5% O_2, with average measurements in human tumors often ranging between 1% and 2% O_2 [134]. This level of oxygenation can still support HIF1α-mediated survival signals while allowing cancer cell proliferation [135, 136]. Our assays, conducted under conditions of mild or physiological hypoxia (2% O_2), demonstrated reductions in *PARP1* and *POLQ* expression, PARylation, and alt-EJ activity. Additionally, cancer cells often exhibit some degree of HIF1α function even under normoxia, which may be driven by the rewiring of oncogenic pathways and metabolism, and increased oxidative stress, among other factors [137–139]. Recognizing that HIF1α generally suppresses alt-EJ reveals a mechanism by which mutagenic DNA repair processes may be exploited to treat HIF1α-driven aggressive cancer phenotypes [140]. These phenotypes are often resistant to DNA-damaging therapies, potentially due to reduced cell proliferation and the modulation of DNA repair pathways [141–143].

The evidence aligns with the frequent amplification and overexpression of *MYC* in HR-deficient breast, ovarian, and prostate tumors [123, 144–146]. Additionally, some PARPi-sensitive but HR-proficient cancers are characterized by *MYC* overexpression [147–149], and this oncogene has been associated with alt-EJ-mediated mutagenesis in leukemias [150]. Furthermore, synthetic lethality between PARP and MYC inhibition, independent of *BRCA1*/*BRCA2* status, has been identified in triple-negative breast cancer [151]. Increased sensitivity to PARPi in MYC-driven cancers may be due to heightened replication stress, resulting in stalled replication forks and DSBs, impaired DSB repair, and/or increased reliance on alternative DNA repair mechanisms [150, 152–156]. Our study expands on these concepts by illustrating the interplay between HIF1α and MYC in the transcriptional regulation of key alt-EJ components, ultimately influencing alt-EJ pathway activity. These findings may also support the evaluation of PARPi and POLθi in tumors exhibiting "high MYC" transcriptional activity, further facilitated by the implemented deep-learning approach. Tumors, or specific regions within tumors, that are, or become, resistant to PARPi or POLθi may exhibit basal activation or acquire activation of HIF1α and/or suppression of MYC. Anticipating these mechanisms could improve therapeutic outcome predictions and guide future combination therapies aimed at overcoming therapeutic resistance.

While our study provides valuable insights into how TGFβ controls transcriptional regulation of alt-EJ by inducing HIFα and suppressing MYC, it is not without limitations. Although consistent molecular associations were observed in tumor data analysis, the findings are primarily derived from *in vitro* and cell-based experiments conducted under specific conditions that do not fully capture the heterogeneity and complexity of tumors. Additionally, studies incorporating a diverse range of cancer cell types with various genetic alterations, alongside complementary assays, are necessary to establish the broader applicability of these results. While we identified significant drug synergism across several settings, definitive causality remains to be confirmed through further mechanistic studies and an expanded repertoire of precision-targeting approaches, including those involving HIF1α. It is also conceivable that other oncogenic signaling pathways suppress alt-EJ, such those increasing cellular stress, causing metabolic rewiring, and/or modulating of DNA damage repair choice. In this context, synergies have been reported with the combined inhibition of PARP and PI3K/mTOR or MEK signaling [157–163]. Addressing these limitations in our study will be critical for validating and extending the clinical relevance of the findings.

Acknowledgements

We would like to thank Oriol Casanovas and Josep Maria Piulats for useful discussions. Our results are partly based upon data generated by the TCGA Research Network

(https://www.cancer.gov/tcga), and we are grateful to the TCGA consortia and coordinators for providing the data and clinical information used here. We are also grateful to Jeremy Stark for providing the U2OS cell lines, to Isabel Puig (VHIO) for providing the shHIF1A, to Laura Soucek and Sandra Martínez (VHIO) for their advice on MYC analysis, and to the investigators who publicly deposited the data used in this work. The anti-HIF1α antibody was a gift from Edurne Berra (CIC bioGUNE).

Author contributions: M.A.P. conceived the study. M.H.B.-H., F.V., A.A., and M.A.P. supervised the study, acquired funding, and wrote the manuscript. R.E. performed bioinformatic, machine and deep learning analyses, and CFC assays. R.E., M.A.P.-C., and I.G. performed bioinformatic analyses. F.M.-J., J.S.-A., S.F.-M., F.M., A.F., A.S., L.R.-A., E.R.-A., I.G., A.B., L.F.-L., A.M.-T., and R.K. performed cellular and molecular analyses. R.T.S. and G.P.V. performed ChIP assays. M.M.-I., X.C.W., E.C., J.A.M., M.L.-C., P.M., I.R., A.R., I.F., A.V., X.S., J.C., M.A., A.H.-R., V.S., K.M., R.H., and J.B. performed data interpretation and provided resources.

Supplementary data

Supplementary data is available at NAR Cancer online.

Conflict of interest

M.H.B.-H. and M.A.P. have filed a patent application, submitted by the University of California and IDIBELL, covering the use of TGFβ and alt-EJ signatures for predicting cancer response to genotoxic therapies.

Funding

This study was funded by the "GINKGO Apac del Berguedà" patient association; the Instituto de Salud Carlos III [co-funded by the European Regional Development Fund (ERDF), "A way to build Europe"] grants PI21/0136 and PI24/01327 to M.A.P., and PI19/00342 and PI23/00513 to A.A.; the Asociación Española Contra el Cáncer (AECC) grant LABAE21170 to A.A.; the Department of Defense PC210340 PCRP-IDA grant to A.A.; the Ministerio de Ciencia, Innovación y Universidades, Agencia Estatal de Investigación [co-funded by the European Regional Development Fund (ERDF), "A way to build Europe"] grants PID2020-117815RB-I00 and PID2023-150836OB-100 to F.V., and CNS2023-145615 to A.A.; and the Generalitat de Catalunya, Agència de Gestió d'Ajuts Universitaris i de Recerca (AGAUR) grants SGR 2017-449 and 2021-00184 to F.V. and M.A.P., and 2021-00895 to A.A. R.E. and M.A.P.-C. were supported by contracts from the Departament de Salut, Generalitat de Catalunya, PERIS-PFI SLT017-20-000076 and PERIS-Suport SLT017/20/000072, respectively, and A.S. was supported by Generalitat de Catalunya AGAUR fellowship 2022-FI-B01068. We also acknowledge the support of the Centres de Recerca de Catalunya (CERCA) Program to IDIBELL and IDIBGI. The open-access publication of this article was funded by the Instituto de Salud Carlos III grants PI24/01327 to M.A.P., PI23/00513 to A.A., and PID2023-150836OB-100 to F.V.

Data availability

The data are available in the article, figures, and additional files. The code for the machine-learning analysis, Bliss synergy scoring, and deep-learning models have been deposited in https://doi.org/10.5281/zenodo.14885044. The MCF10A microarray data were deposited in GEO reference GSE8240.

References

1. Chapman JR, Taylor MRG, Boulton SJ. Playing the end game: DNA double-strand break repair pathway choice. *Mol Cell* 2012;**47**:497–510. https://doi.org/10.1016/j.molcel.2012.07.029
2. Jasin M, Rothstein R. Repair of strand breaks by homologous recombination. *Cold Spring Harb Perspect Biol* 2013;**5**:a012740. https://doi.org/10.1101/cshperspect.a012740
3. Scully R, Panday A, Elango R *et al.* DNA double-strand break repair-pathway choice in somatic mammalian cells. *Nat Rev Mol Cell Biol* 2019;**20**:698–714. https://doi.org/10.1038/s41580-019-0152-0
4. Miki Y, Swensen J, Shattuck-Eidens D *et al.* A strong candidate for the breast and ovarian cancer susceptibility gene *BRCA1*. *Science* 1994;**266**:66–71. https://doi.org/10.1126/science.7545954
5. Wooster R, Bignell G, Lancaster J *et al.* Identification of the breast cancer susceptibility gene *BRCA2*. *Nature* 1995;**378**:789–92. https://doi.org/10.1038/378789a0
6. Prakash R, Zhang Y, Feng W *et al.* Homologous recombination and human health: the roles of BRCA1, BRCA2, and associated proteins. *Cold Spring Harb Perspect Biol* 2015;**7**:a016600. https://doi.org/10.1101/cshperspect.a016600
7. Bryant HE, Schultz N, Thomas HD *et al.* Specific killing of BRCA2-deficient tumours with inhibitors of poly(ADP-ribose) polymerase. *Nature* 2005;**434**:913–7. https://doi.org/10.1038/nature03443
8. Farmer H, McCabe N, Lord CJ *et al.* Targeting the DNA repair defect in *BRCA* mutant cells as a therapeutic strategy. *Nature* 2005;**434**:917–21. https://doi.org/10.1038/nature03445
9. Sfeir A, Symington LS. Microhomology-mediated end joining: a back-up survival mechanism or dedicated pathway? *Trends Biochem Sci* 2015;**40**:701–14. https://doi.org/10.1016/j.tibs.2015.08.006
10. Ceccaldi R, Liu JC, Amunugama R *et al.* Homologous-recombination-deficient tumours are dependent on Polθ-mediated repair. *Nature* 2015;**518**:258–62. https://doi.org/10.1038/nature14184
11. Ceccaldi R, Rondinelli B, D'Andrea AD. Repair pathway choices and consequences at the double-strand break. *Trends Cell Biol* 2016;**26**:52–64. https://doi.org/10.1016/j.tcb.2015.07.009
12. Chang HHY, Pannunzio NR, Adachi N *et al.* Non-homologous DNA end joining and alternative pathways to double-strand break repair. *Nat Rev Mol Cell Biol* 2017;**18**:495–506. https://doi.org/10.1038/nrm.2017.48
13. Brambati A, Barry RM, Sfeir A. DNA polymerase theta (Polθ)—an error-prone polymerase necessary for genome stability. *Curr Opin Genet Dev* 2020;**60**:119–26. https://doi.org/10.1016/j.gde.2020.02.017
14. Lord CJ, Ashworth A. PARP inhibitors: synthetic lethality in the clinic. *Science* 2017;**355**:1152–8. https://doi.org/10.1126/science.aam7344
15. Fong PC, Boss DS, Yap TA *et al.* Inhibition of poly(ADP-ribose) polymerase in tumors from *BRCA* mutation carriers. *N Engl J Med* 2009;**361**:123–34. https://doi.org/10.1056/NEJMoa0900212
16. Ledermann J, Harter P, Gourley C *et al.* Olaparib maintenance therapy in platinum-sensitive relapsed ovarian cancer. *N Engl J Med* 2012;**366**:1382–92. https://doi.org/10.1056/NEJMoa1105535

17. Hoppe MM, Sundar R, Tan DSP *et al.* Biomarkers for homologous recombination deficiency in cancer. *J Natl Cancer Inst* 2018;**110**:704–13. https://doi.org/10.1093/jnci/djy085
18. de Bono J, Mateo J, Fizazi K *et al.* Olaparib for metastatic castration-resistant prostate cancer. *N Engl J Med* 2020;**382**:2091–102. https://doi.org/10.1056/NEJMoa1911440
19. Miller RE, Leary A, Scott CL *et al.* ESMO recommendations on predictive biomarker testing for homologous recombination deficiency and PARP inhibitor benefit in ovarian cancer. *Ann Oncol* 2020;**31**:1606–22. https://doi.org/10.1016/j.annonc.2020.08.2102
20. Tew WP, Lacchetti C, Ellis A *et al.* PARP inhibitors in the management of ovarian cancer: ASCO guideline. *JCO* 2020;**38**:3468–93. https://doi.org/10.1200/JCO.20.01924
21. Tutt ANJ, Garber JE, Kaufman B *et al.* Adjuvant olaparib for patients with *BRCA1*- or *BRCA2*-mutated breast cancer. *N Engl J Med* 2021;**384**:2394–405. https://doi.org/10.1056/NEJMoa2105215
22. Schrempf A, Slyskova J, Loizou JI. Targeting the DNA repair enzyme polymerase θ in cancer therapy. *Trends Cancer* 2021;**7**:98–111. https://doi.org/10.1016/j.trecan.2020.09.007
23. Zatreanu D, Robinson HMR, Alkhatib O *et al.* Polθ inhibitors elicit *BRCA*-gene synthetic lethality and target PARP inhibitor resistance. *Nat Commun* 2021;**12**:3636. https://doi.org/10.1038/s41467-021-23463-8
24. Zhou J, Gelot C, Pantelidou C *et al.* A first-in-class polymerase theta inhibitor selectively targets homologous-recombination-deficient tumors. *Nat Cancer* 2021;**2**:598–610. https://doi.org/10.1038/s43018-021-00203-x
25. Ramsden DA, Carvajal-Garcia J, Gupta GP. Mechanism, cellular functions and cancer roles of polymerase-theta-mediated DNA end joining. *Nat Rev Mol Cell Biol* 2022;**23**:125–40. https://doi.org/10.1038/s41580-021-00405-2
26. Patterson-Fortin J, D'Andrea AD. Targeting polymerase theta (POLθ) for cancer therapy. *Cancer Treat Res* 2023;**186**:285–98. https://doi.org/10.1007/978-3-031-30065-3_15
27. Iliakis G, Murmann T, Soni A. Alternative end-joining repair pathways are the ultimate backup for abrogated classical non-homologous end-joining and homologous recombination repair: implications for the formation of chromosome translocations. *Mutat Res Genet Toxicol Environ Mutagen* 2015;**793**:166–75. https://doi.org/10.1016/j.mrgentox.2015.07.001
28. Ahrabi S, Sarkar S, Pfister SX *et al.* A role for human homologous recombination factors in suppressing microhomology-mediated end joining. *Nucleic Acids Res* 2016;**44**:5743–57. https://doi.org/10.1093/nar/gkw326
29. Kirshner J, Jobling MF, Pajares MJ *et al.* Inhibition of transforming growth factor-beta1 signaling attenuates ataxia telangiectasia mutated activity in response to genotoxic stress. *Cancer Res* 2006;**66**:10861–9. https://doi.org/10.1158/0008-5472.CAN-06-2565
30. Martinez-Ruiz H, Illa-Bochaca I, Omene C *et al.* A TGFβ-miR-182-BRCA1 axis controls the mammary differentiation hierarchy. *Sci Signal* 2016;**9**:ra118. https://doi.org/10.1126/scisignal.aaf5402
31. Zhang H, Kozono DE, O'Connor KW *et al.* TGF-β inhibition rescues hematopoietic stem cell defects and bone marrow failure in Fanconi anemia. *Cell Stem Cell* 2016;**18**:668–81. https://doi.org/10.1016/j.stem.2016.03.002
32. Chen J, Shukla V, Farci P *et al.* Loss of the transforming growth factor-β effector β2-spectrin promotes genomic instability. *Hepatology* 2017;**65**:678–93. https://doi.org/10.1002/hep.28927
33. Liu Q, Ma L, Jones T *et al.* Subjugation of TGFβ signaling by human papilloma virus in head and neck squamous cell carcinoma shifts DNA repair from homologous recombination to alternative end-joining. *Clin Cancer Res* 2018;**24**:6001–14. https://doi.org/10.1158/1078-0432.CCR-18-1346
34. Liu Q, Lopez K, Murnane J *et al.* Misrepair in context: TGFβ regulation of DNA repair. *Front Oncol* 2019;**9**:799. https://doi.org/10.3389/fonc.2019.00799
35. Liu Q, Palomero L, Moore J *et al.* Loss of TGFβ signaling increases alternative end-joining DNA repair that sensitizes to genotoxic therapies across cancer types. *Sci Transl Med* 2021;**13**:eabc4465. https://doi.org/10.1126/scitranslmed.abc4465
36. Guix I, Liu Q, Pujana MA *et al.* Validation of anticorrelated TGFβ signaling and alternative end-joining DNA repair signatures that predict response to genotoxic cancer therapy. *Clin Cancer Res* 2022;**28**:1372–82. https://doi.org/10.1158/1078-0432.CCR-21-2846
37. Liu J, Lichtenberg T, Hoadley KA *et al.* An integrated TCGA pan-cancer clinical data resource to drive high-quality survival outcome analytics. *Cell* 2018;**173**:400–16. https://doi.org/10.1016/j.cell.2018.02.052
38. Cerami E, Gao J, Dogrusoz U *et al.* The cBio cancer genomics portal: an open platform for exploring multidimensional cancer genomics data. *Cancer Discov* 2012;**2**:401–4. https://doi.org/10.1158/2159-8290.CD-12-0095
39. Telli ML, Timms KM, Reid J *et al.* Homologous recombination deficiency (HRD) score predicts response to platinum-containing neoadjuvant chemotherapy in patients with triple-negative breast cancer. *Clin Cancer Res* 2016;**22**:3764–73. https://doi.org/10.1158/1078-0432.CCR-15-2477
40. Rempel E, Kluck K, Beck S *et al.* Pan-cancer analysis of genomic scar patterns caused by homologous repair deficiency (HRD). *NPJ Precis Oncol* 2022;**6**:36. https://doi.org/10.1038/s41698-022-00276-6
41. Chakravarty D, Gao J, Phillips SM *et al.* OncoKB: a precision oncology knowledge base. *JCO Precis Oncol* 2017;**2017**:PO.17.00011.
42. Cook DP, Vanderhyden BC. Context specificity of the EMT transcriptional response. *Nat Commun* 2020;**11**:2142. https://doi.org/10.1038/s41467-020-16066-2
43. Andrysik Z, Bender H, Galbraith MD *et al.* Multi-omics analysis reveals contextual tumor suppressive and oncogenic gene modules within the acute hypoxic response. *Nat Commun* 2021;**12**:1375. https://doi.org/10.1038/s41467-021-21687-2
44. Ghandi M, Huang FW, Jané-Valbuena J *et al.* Next-generation characterization of the Cancer Cell Line Encyclopedia. *Nature* 2019;**569**:503–8. https://doi.org/10.1038/s41586-019-1186-3
45. Tsherniak A, Vazquez F, Montgomery PG *et al.* Defining a cancer dependency map. *Cell* 2017;**170**:564–76.
46. Corsello SM, Nagari RT, Spangler RD *et al.* Discovering the anti-cancer potential of non-oncology drugs by systematic viability profiling. *Nat Cancer* 2020;**1**:235–48. https://doi.org/10.1038/s43018-019-0018-6
47. Garnett MJ, Edelman EJ, Heidorn SJ *et al.* Systematic identification of genomic markers of drug sensitivity in cancer cells. *Nature* 2012;**483**:570–5. https://doi.org/10.1038/nature11005
48. Iorio F, Knijnenburg TA, Vis DJ *et al.* A landscape of pharmacogenomic interactions in cancer. *Cell* 2016;**166**:740–54. https://doi.org/10.1016/j.cell.2016.06.017
49. Picco G, Chen ED, Alonso LG *et al.* Functional linkage of gene fusions to cancer cell fitness assessed by pharmacological and CRISPR–Cas9 screening. *Nat Commun* 2019;**10**:2198. https://doi.org/10.1038/s41467-019-09940-1
50. Nusinow DP, Szpyt J, Ghandi M *et al.* Quantitative proteomics of the Cancer Cell Line Encyclopedia. *Cell* 2020;**180**:387–402. https://doi.org/10.1016/j.cell.2019.12.023
51. Gonçalves E, Poulos RC, Cai Z *et al.* Pan-cancer proteomic map of 949 human cell lines. *Cancer Cell* 2022;**40**:835–49. https://doi.org/10.1016/j.ccell.2022.06.010
52. Thorndike R. Who belongs in the family? *Psychometrika* 1953;**18**:267–76. https://doi.org/10.1007/BF02289263

53. Li J, Liu W, Mojumdar K *et al.* A protein expression atlas on tissue samples and cell lines from cancer patients provides insights into tumor heterogeneity and dependencies. *Nat Cancer* 2024;**5**:1579–95. https://doi.org/10.1038/s43018-024-00817-x
54. Kueckelhaus J, Frerich S, Kada-Benotmane J *et al.* Inferring histology-associated gene expression gradients in spatial transcriptomic studies. *Nat Commun* 2024;**15**:7280. https://doi.org/10.1038/s41467-024-50904-x
55. Ravi VM, Will P, Kueckelhaus J *et al.* Spatially resolved multi-omics deciphers bidirectional tumor-host interdependence in glioblastoma. *Cancer Cell* 2022;**40**:639–55. https://doi.org/10.1016/j.ccell.2022.05.009
56. Buffa FM, Harris AL, West CM *et al.* Large meta-analysis of multiple cancers reveals a common, compact and highly prognostic hypoxia metagene. *Br J Cancer* 2010;**102**:428–35. https://doi.org/10.1038/sj.bjc.6605450
57. Fox NS, Starmans MHW, Haider S *et al.* Ensemble analyses improve signatures of tumour hypoxia and reveal inter-platform differences. *BMC Bioinformatics* 2014;**15**:170. https://doi.org/10.1186/1471-2105-15-170
58. Kim J, Woo AJ, Chu J *et al.* A Myc rather than core pluripotency module accounts for the shared signatures of embryonic stem and cancer cells. *Cell* 2010;**143**:313–24. https://doi.org/10.1016/j.cell.2010.09.010
59. Hänzelmann S, Castelo R, Guinney J. GSVA: gene set variation analysis for microarray and RNA-seq data. *BMC Bioinformatics* 2013;**14**:7. https://doi.org/10.1186/1471-2105-14-7
60. Lee DD, Seung HS. Learning the parts of objects by non-negative matrix factorization. *Nature* 1999;**401**:788–91. https://doi.org/10.1038/44565
61. Perou CM, Sørlie T, Eisen MB *et al.* Molecular portraits of human breast tumours. *Nature* 2000;**406**:747–52. https://doi.org/10.1038/35021093
62. Glorot X, Bordes A, Bengio Y. Deep sparse rectifier neural networks. In: *Proceedingsof the Fourteenth International Conference on Artificial Intelligence andStatistics*, Proceedingsof Machine Learning Research Series, Vol. **15**. FortLauderdale, FL, USA: PMLR, 2011, 315–23.
63. Srivastava N, Hinton G, Krizhevsky A *et al.* Dropout: a simple way to prevent neural networks from overfitting. *J Mach Learn Res* 2014;**15**:1929–58.
64. Kingma DP, Ba J. Adam: a method for stochastic optimization. arXiv, https://arxiv.org/abs/1412.6980, 30 January 2017, preprint: not peer reviewed.
65. Prechelt L. Early stopping-but when? In: *Neural Networks: Tricks of the Trade*, Vol. **1524**. Berlin, Heidelberg: Springer Berlin Heidelberg, 2002, 55–69.
66. Lundberg SM, Lee S-I. A unified approach to interpreting model predictions. In: *Proceedings of the 31st International Conference on Neural Information Processing Systems, NIPS'17*. Long Beach, California, USA: Curran Associates Inc., 2017, 4768–77.
67. Subramanian A, Tamayo P, Mootha VK *et al.* Gene set enrichment analysis: a knowledge-based approach for interpreting genome-wide expression profiles. *Proc Natl Acad Sci USA* 2005;**102**:15545–50. https://doi.org/10.1073/pnas.0506580102
68. Whitfield ML, Sherlock G, Saldanha AJ *et al.* Identification of genes periodically expressed in the human cell cycle and their expression in tumors. *MBoC* 2002;**13**:1977–2000. https://doi.org/10.1091/mbc.02-02-0030
69. Andarawewa KL, Erickson AC, Chou WS *et al.* Ionizing radiation predisposes nonmalignant human mammary epithelial cells to undergo transforming growth factor beta induced epithelial to mesenchymal transition. *Cancer Res* 2007;**67**:8662–70. https://doi.org/10.1158/0008-5472.CAN-07-1294
70. Livak KJ, Schmittgen TD. Analysis of relative gene expression data using real-time quantitative PCR and the 2(-Delta Delta C(T)) method. *Methods* 2001;**25**:402–8. https://doi.org/10.1006/meth.2001.1262
71. Berra E, Richard DE, Gothié E *et al.* HIF-1-dependent transcriptional activity is required for oxygen-mediated HIF-1alpha degradation. *FEBS Lett* 2001;**491**:85–90. https://doi.org/10.1016/S0014-5793(01)02159-7
72. Gunn A, Stark JM. I-SceI-based assays to examine distinct repair outcomes of mammalian chromosomal double strand breaks. *Methods Mol Biol* 2012;**920**:379–91. https://doi.org/10.1007/978-1-61779-998-3_27
73. Bliss C. The toxicity of poisons applied jointly. *Ann Appl Biol* 1939;**26**:585–615. https://doi.org/10.1111/j.1744-7348.1939.tb06990.x
74. Ianevski A, Giri AK, Aittokallio T. SynergyFinder 2.0: visual analytics of multi-drug combination synergies. *Nucleic Acids Res* 2020;**48**:W488–93. https://doi.org/10.1093/nar/gkaa216
75. Di Veroli GY, Fornari C, Wang D *et al.* Combenefit: an interactive platform for the analysis and visualization of drug combinations. *Bioinformatics* 2016;**32**:2866–8. https://doi.org/10.1093/bioinformatics/btw230
76. Maxwell CA, Benítez J, Gómez-Baldó L *et al.* Interplay between BRCA1 and RHAMM regulates epithelial apicobasal polarization and may influence risk of breast cancer. *PLoS Biol* 2011;**9**:e1001199. https://doi.org/10.1371/journal.pbio.1001199
77. Cuesta-Borràs E, Salvans C, Arqués O *et al.* DPPA3-HIF1α axis controls colorectal cancer chemoresistance by imposing a slow cell-cycle phenotype. *Cell Rep* 2023;**42**:112927. https://doi.org/10.1016/j.celrep.2023.112927
78. Strutt H, Paro R. Mapping DNA target sites of chromatin proteins *in vivo* by formaldehyde crosslinking. *Methods Mol Biol* 1999;**119**:455–67.
79. Lu MY, Williamson DFK, Chen TY *et al.* Data-efficient and weakly supervised computational pathology on whole-slide images. *Nat Biomed Eng* 2021;**5**:555–70. https://doi.org/10.1038/s41551-020-00682-w
80. Chen RJ, Ding T, Lu MY *et al.* Towards a general-purpose foundation model for computational pathology. *Nat Med* 2024;**30**:850–62. https://doi.org/10.1038/s41591-024-02857-3
81. Higgins GS, Harris AL, Prevo R *et al.* Overexpression of *POLQ* confers a poor prognosis in early breast cancer patients. *Oncotarget* 2010;**1**:175–84. https://doi.org/10.18632/oncotarget.124
82. Mateos-Gomez PA, Gong F, Nair N *et al.* Mammalian polymerase θ promotes alternative NHEJ and suppresses recombination. *Nature* 2015;**518**:254–7. https://doi.org/10.1038/nature14157
83. Lemée F, Bergoglio V, Fernandez-Vidal A *et al.* DNA polymerase theta up-regulation is associated with poor survival in breast cancer, perturbs DNA replication, and promotes genetic instability. *Proc Natl Acad Sci USA* 2010;**107**:13390–5. https://doi.org/10.1073/pnas.0910759107
84. Syed A, Filandr F, Patterson-Fortin J *et al.* Novobiocin blocks nucleic acid binding to Polθ and inhibits stimulation of its ATPase activity. *Nucleic Acids Res* 2023;**51**:9920–37. https://doi.org/10.1093/nar/gkad727
85. Brunet J-P, Tamayo P, Golub TR *et al.* Metagenes and molecular pattern discovery using matrix factorization. *Proc Natl Acad Sci USA* 2004;**101**:4164–9. https://doi.org/10.1073/pnas.0308531101
86. Bai F, Smith MD, Chan HL *et al.* Germline mutation of *Brca1* alters the fate of mammary luminal cells and causes luminal-to-basal mammary tumor transformation. *Oncogene* 2013;**32**:2715–25. https://doi.org/10.1038/onc.2012.293
87. Bai F, Chan HL, Scott A *et al.* BRCA1 suppresses epithelial-to-mesenchymal transition and stem cell dedifferentiation during mammary and tumor development. *Cancer Res* 2014;**74**:6161–72. https://doi.org/10.1158/0008-5472.CAN-14-1119
88. Wang H, Xiang D, Liu B *et al.* Inadequate DNA damage repair promotes mammary transdifferentiation, leading to BRCA1

breast cancer. *Cell* 2019;**178**:135–51. https://doi.org/10.1016/j.cell.2019.06.002
89. Bai F, Wang C, Liu X *et al.* Loss of function of BRCA1 promotes EMT in mammary tumors through activation of TGFβR2 signaling pathway. *Cell Death Dis* 2022;**13**:195. https://doi.org/10.1038/s41419-022-04646-7
90. Secombe J, Pierce SB, Eisenman RN. Myc: a weapon of mass destruction. *Cell* 2004;**117**:153–6. https://doi.org/10.1016/S0092-8674(04)00336-8
91. Chen H-Z, Tsai S-Y, Leone G. Emerging roles of E2Fs in cancer: an exit from cell cycle control. *Nat Rev Cancer* 2009;**9**:785–97. https://doi.org/10.1038/nrc2696
92. Shih SC, Claffey KP. Role of AP-1 and HIF-1 transcription factors in TGF-beta activation of VEGF expression. *Growth Factors* 2001;**19**:19–34. https://doi.org/10.3109/08977190109001073
93. Görlach A, Diebold I, Schini-Kerth VB *et al.* Thrombin activates the hypoxia-inducible factor-1 signaling pathway in vascular smooth muscle cells: role of the p22(phox)-containing NADPH oxidase. *Circ Res* 2001;**89**:47–54. https://doi.org/10.1161/hh1301.092678
94. McMahon S, Charbonneau M, Grandmont S *et al.* Transforming growth factor beta1 induces hypoxia-inducible factor-1 stabilization through selective inhibition of PHD2 expression. *J Biol Chem* 2006;**281**:24171–81. https://doi.org/10.1074/jbc.M604507200
95. Hanna C, Hubchak SC, Liang X *et al.* Hypoxia-inducible factor-2α and TGF-β signaling interact to promote normoxic glomerular fibrogenesis. *Am J Physiol Renal Physiol* 2013;**305**:F1323–31. https://doi.org/10.1152/ajprenal.00155.2013
96. Kaelin WG. The von Hippel–Lindau tumour suppressor protein: O2 sensing and cancer. *Nat Rev Cancer* 2008;**8**:865–73. https://doi.org/10.1038/nrc2502
97. Suehnholz SP, Nissan MH, Zhang H *et al.* Quantifying the expanding landscape of clinical actionability for patients with cancer. *Cancer Discov* 2024;**14**:49–65. https://doi.org/10.1158/2159-8290.CD-23-0467
98. Gibson BA, Kraus WL. New insights into the molecular and cellular functions of poly(ADP-ribose) and PARPs. *Nat Rev Mol Cell Biol* 2012;**13**:411–24. https://doi.org/10.1038/nrm3376
99. Audebert M, Salles B, Calsou P. Involvement of poly(ADP-ribose) polymerase-1 and XRCC1/DNA ligase III in an alternative route for DNA double-strand breaks rejoining. *J Biol Chem* 2004;**279**:55117–26. https://doi.org/10.1074/jbc.M404524200
100. Tobin LA, Robert C, Rapoport AP *et al.* Targeting abnormal DNA double-strand break repair in tyrosine kinase inhibitor-resistant chronic myeloid leukemias. *Oncogene* 2013;**32**:1784–93. https://doi.org/10.1038/onc.2012.203
101. Howard SM, Yanez DA, Stark JM. DNA damage response factors from diverse pathways, including DNA crosslink repair, mediate alternative end joining. *PLoS Genet* 2015;**11**:e1004943. https://doi.org/10.1371/journal.pgen.1004943
102. Welsh S, Williams R, Kirkpatrick L *et al.* Antitumor activity and pharmacodynamic properties of PX-478, an inhibitor of hypoxia-inducible factor-1alpha. *Mol Cancer Ther* 2004;**3**:233–44. https://doi.org/10.1158/1535-7163.233.3.3
103. Schwartz DL, Powis G, Thitai-Kumar A *et al.* The selective hypoxia inducible factor-1 inhibitor PX-478 provides *in vivo* radiosensitization through tumor stromal effects. *Mol Cancer Ther* 2009;**8**:947–58. https://doi.org/10.1158/1535-7163.MCT-08-0981
104. Schwartz DL, Bankson JA, Lemos R *et al.* Radiosensitization and stromal imaging response correlates for the HIF-1 inhibitor PX-478 given with or without chemotherapy in pancreatic cancer. *Mol Cancer Ther* 2010;**9**:2057–67. https://doi.org/10.1158/1535-7163.MCT-09-0768
105. Wang B-F, Wang X-J, Kang H-F *et al.* Saikosaponin-D enhances radiosensitivity of hepatoma cells under hypoxic conditions by inhibiting hypoxia-inducible factor-1α. *Cell Physiol Biochem* 2014;**33**:37–51. https://doi.org/10.1159/000356648
106. Zou Z, Ohta T, Miura F *et al.* ChIP-Atlas 2021 update: a data-mining suite for exploring epigenomic landscapes by fully integrating ChIP-seq, ATAC-seq and bisulfite-seq data. *Nucleic Acids Res* 2022;**50**:W175–82. https://doi.org/10.1093/nar/gkac199
107. Maeda M, Johnson KR, Wheelock MJ. Cadherin switching: essential for behavioral but not morphological changes during an epithelium-to-mesenchyme transition. *J Cell Sci* 2005;**118**:873–87. https://doi.org/10.1242/jcs.01634
108. Daly CS, Flemban A, Shafei M *et al.* Hypoxia modulates the stem cell population and induces EMT in the MCF-10A breast epithelial cell line. *Oncol Rep* 2018;**39**:483–90.
109. Deshmukh AP, Vasaikar SV, Tomczak K *et al.* Identification of EMT signaling cross-talk and gene regulatory networks by single-cell RNA sequencing. *Proc Natl Acad Sci USA* 2021;**118**:e2102050118. https://doi.org/10.1073/pnas.2102050118
110. Koshiji M, To KK-W, Hammer S *et al.* HIF-1alpha induces genetic instability by transcriptionally downregulating MutSalpha expression. *Mol Cell* 2005;**17**:793–803. https://doi.org/10.1016/j.molcel.2005.02.015
111. Meng AX, Jalali F, Cuddihy A *et al.* Hypoxia down-regulates DNA double strand break repair gene expression in prostate cancer cells. *Radiother Oncol* 2005;**76**:168–76. https://doi.org/10.1016/j.radonc.2005.06.025
112. Semenza GL. Hypoxia-inducible factors in physiology and medicine. *Cell* 2012;**148**:399–408. https://doi.org/10.1016/j.cell.2012.01.021
113. Yang W, Soares J, Greninger P *et al.* Genomics of Drug Sensitivity in Cancer (GDSC): a resource for therapeutic biomarker discovery in cancer cells. *Nucleic Acids Res* 2013;**41**:D955–61. https://doi.org/10.1093/nar/gks1111
114. Maxwell PH. The HIF pathway in cancer. *Semin Cell Dev Biol* 2005;**16**:523–30. https://doi.org/10.1016/j.semcdb.2005.03.001
115. Burlison JA, Neckers L, Smith AB *et al.* Novobiocin: redesigning a DNA gyrase inhibitor for selective inhibition of hsp90. *J Am Chem Soc* 2006;**128**:15529–36. https://doi.org/10.1021/ja065793p
116. Donnelly A, Blagg BSJ. Novobiocin and additional inhibitors of the Hsp90 C-terminal nucleotide-binding pocket. *Curr Med Chem* 2008;**15**:2702–17. https://doi.org/10.2174/092986708786242895
117. Audisio D, Methy-Gonnot D, Radanyi C *et al.* Synthesis and antiproliferative activity of novobiocin analogues as potential hsp90 inhibitors. *Eur J Med Chem* 2014;**83**:498–507. https://doi.org/10.1016/j.ejmech.2014.06.067
118. Ronson GE, Starowicz K, Anthony EJ *et al.* Mechanisms of synthetic lethality between BRCA1/2 and 53BP1 deficiencies and DNA polymerase theta targeting. *Nat Commun* 2023;**14**:7834. https://doi.org/10.1038/s41467-023-43677-2
119. Sullivan-Reed K, Toma MM, Drzewiecka M *et al.* Simultaneous targeting of DNA polymerase theta and PARP1 or RAD52 triggers dual synthetic lethality in homologous recombination-deficient leukemia cells. *Mol Cancer Res* 2023;**21**:1017–22. https://doi.org/10.1158/1541-7786.MCR-22-1035
120. Mangraviti A, Raghavan T, Volpin F *et al.* HIF-1α-targeting acriflavine provides long term survival and radiological tumor response in brain cancer therapy. *Sci Rep* 2017;**7**:14978. https://doi.org/10.1038/s41598-017-14990-w
121. Sallais J, Park C, Alahari S *et al.* HIF1 inhibitor acriflavine rescues early-onset preeclampsia phenotype in mice lacking placental prolyl hydroxylase domain protein 2. *JCI Insight* 2022;**7**:e158908. https://doi.org/10.1172/jci.insight.158908
122. Palayoor ST, Mitchell JB, Cerna D *et al.* PX-478, an inhibitor of hypoxia-inducible factor-1alpha, enhances radiosensitivity of

prostate carcinoma cells. *Int J Cancer* 2008;**123**:2430–7. https://doi.org/10.1002/ijc.23807
123. Cancer Genome Atlas Research Network. Integrated genomic analyses of ovarian carcinoma. *Nature* 2011;**474**:609–15. https://doi.org/10.1038/nature10166
124. Cancer Genome Atlas Research Network. The molecular taxonomy of primary prostate cancer. *Cell* 2015;**163**:1011–25. https://doi.org/10.1016/j.cell.2015.10.025
125. Liu X, Ge Z, Yang F *et al.* Identification of biomarkers of response to preoperative talazoparib monotherapy in treatment naïve g*BRCA*+ breast cancers. *NPJ Breast Cancer* 2022;**8**:64. https://doi.org/10.1038/s41523-022-00427-9
126. França GS, Baron M, King BR *et al.* Cellular adaptation to cancer therapy along a resistance continuum. *Nature* 2024;**631**:876–83. https://doi.org/10.1038/s41586-024-07690-9
127. Wicks EE, Semenza GL. Hypoxia-inducible factors: cancer progression and clinical translation. *J Clin Invest* 2022;**132**:e159839. https://doi.org/10.1172/JCI159839
128. Liu J, Gao Y, Zhang X. A patent review on hypoxia-inducible factor (HIF) modulators (2021-2023). *Expert Opin Ther Pat* 2024;**34**:651–64. https://doi.org/10.1080/13543776.2024.2368739
129. Gordan JD, Thompson CB, Simon MC. HIF and c-myc: sibling rivals for control of cancer cell metabolism and proliferation. *Cancer Cell* 2007;**12**:108–13. https://doi.org/10.1016/j.ccr.2007.07.006
130. Dang CV, Kim J, Gao P *et al.* The interplay between MYC and HIF in cancer. *Nat Rev Cancer* 2008;**8**:51–6. https://doi.org/10.1038/nrc2274
131. Li Y, Sun X-X, Qian DZ *et al.* Molecular crosstalk between MYC and HIF in cancer. *Front Cell Dev Biol* 2020;**8**:590576. https://doi.org/10.3389/fcell.2020.590576
132. Koshiji M, Kageyama Y, Pete EA *et al.* HIF-1alpha induces cell cycle arrest by functionally counteracting Myc. *EMBO J* 2004;**23**:1949–56. https://doi.org/10.1038/sj.emboj.7600196
133. To KK-W, Sedelnikova OA, Samons M *et al.* The phosphorylation status of PAS-B distinguishes HIF-1alpha from HIF-2alpha in NBS1 repression. *EMBO J* 2006;**25**:4784–94. https://doi.org/10.1038/sj.emboj.7601369
134. McKeown SR. Defining normoxia, physoxia and hypoxia in tumours-implications for treatment response. *Br J Radiol* 2014;**87**:20130676. https://doi.org/10.1259/bjr.20130676
135. Jiang BH, Semenza GL, Bauer C *et al.* Hypoxia-inducible factor 1 levels vary exponentially over a physiologically relevant range of O2 tension. *Am J Physiol* 1996;**271**:C1172–80. https://doi.org/10.1152/ajpcell.1996.271.4.C1172
136. Bertout JA, Patel SA, Simon MC. The impact of O2 availability on human cancer. *Nat Rev Cancer* 2008;**8**:967–75. https://doi.org/10.1038/nrc2540
137. Pagé EL, Robitaille GA, Pouysségur J *et al.* Induction of hypoxia-inducible factor-1alpha by transcriptional and translational mechanisms. *J Biol Chem* 2002;**277**:48403–9. https://doi.org/10.1074/jbc.M209114200
138. Kaelin WG. ROS: really involved in oxygen sensing. *Cell Metab* 2005;**1**:357–8. https://doi.org/10.1016/j.cmet.2005.05.006
139. Semenza GL. HIF-1 mediates metabolic responses to intratumoral hypoxia and oncogenic mutations. *J Clin Invest* 2013;**123**:3664–71. https://doi.org/10.1172/JCI67230
140. Vaupel P. Hypoxia and aggressive tumor phenotype: implications for therapy and prognosis. *Oncologist* 2008;**13**:21–6. https://doi.org/10.1634/theoncologist.13-S3-21
141. Bristow RG, Hill RP. Hypoxia and metabolism. Hypoxia, DNA repair and genetic instability. *Nat Rev Cancer* 2008;**8**:180–92. https://doi.org/10.1038/nrc2344
142. Wilson WR, Hay MP. Targeting hypoxia in cancer therapy. *Nat Rev Cancer* 2011;**11**:393–410. https://doi.org/10.1038/nrc3064
143. Scanlon SE, Glazer PM. Multifaceted control of DNA repair pathways by the hypoxic tumor microenvironment. *DNA Repair (Amst)* 2015;**32**:180–9. https://doi.org/10.1016/j.dnarep.2015.04.030
144. Grushko TA, Dignam JJ, Das S *et al.* *MYC* is amplified in *BRCA1*-associated breast cancers. *Clin Cancer Res* 2004;**10**:499–507. https://doi.org/10.1158/1078-0432.CCR-0976-03
145. Castro E, Jugurnauth-Little S, Karlsson Q *et al.* High burden of copy number alterations and *c-MYC* amplification in prostate cancer from *BRCA2* germline mutation carriers. *Ann Oncol* 2015;**26**:2293–300. https://doi.org/10.1093/annonc/mdv356
146. Li C, Bonazzoli E, Bellone S *et al.* Mutational landscape of primary, metastatic, and recurrent ovarian cancer reveals *c-MYC* gains as potential target for BET inhibitors. *Proc Natl Acad Sci USA* 2019;**116**:619–24. https://doi.org/10.1073/pnas.1814027116
147. Caracciolo D, Scionti F, Juli G *et al.* Exploiting MYC-induced PARPness to target genomic instability in multiple myeloma. *Haematologica* 2021;**106**:185–95. https://doi.org/10.3324/haematol.2019.240713
148. Ning J-F, Stanciu M, Humphrey MR *et al.* Myc targeted CDK18 promotes ATR and homologous recombination to mediate PARP inhibitor resistance in glioblastoma. *Nat Commun* 2019;**10**:2910. https://doi.org/10.1038/s41467-019-10993-5
149. Yi J, Liu C, Tao Z *et al.* MYC status as a determinant of synergistic response to Olaparib and Palbociclib in ovarian cancer. *EBioMedicine* 2019;**43**:225–37. https://doi.org/10.1016/j.ebiom.2019.03.027
150. Muvarak N, Kelley S, Robert C *et al.* c-MYC generates repair errors via increased transcription of alternative-NHEJ factors, LIG3 and PARP1, in tyrosine kinase-activated leukemias. *Mol Cancer Res* 2015;**13**:699–712. https://doi.org/10.1158/1541-7786.MCR-14-0422
151. Carey JPW, Karakas C, Bui T *et al.* Synthetic lethality of PARP inhibitors in combination with MYC blockade is independent of *BRCA* status in triple-negative breast cancer. *Cancer Res* 2018;**78**:742–57. https://doi.org/10.1158/0008-5472.CAN-17-1494
152. Vafa O, Wade M, Kern S *et al.* c-Myc can induce DNA damage, increase reactive oxygen species, and mitigate p53 function: a mechanism for oncogene-induced genetic instability. *Mol Cell* 2002;**9**:1031–44. https://doi.org/10.1016/S1097-2765(02)00520-8
153. Karlsson A, Deb-Basu D, Cherry A *et al.* Defective double-strand DNA break repair and chromosomal translocations by *MYC* overexpression. *Proc Natl Acad Sci USA* 2003;**100**:9974–9. https://doi.org/10.1073/pnas.1732638100
154. Dominguez-Sola D, Ying CY, Grandori C *et al.* Non-transcriptional control of DNA replication by c-Myc. *Nature* 2007;**448**:445–51. https://doi.org/10.1038/nature05953
155. Li Z, Owonikoko TK, Sun S-Y *et al.* c-Myc suppression of DNA double-strand break repair. *Neoplasia* 2012;**14**:1190–202. https://doi.org/10.1593/neo.121258
156. Kotsantis P, Petermann E, Boulton SJ. Mechanisms of oncogene-induced replication stress: jigsaw falling into place. *Cancer Discov* 2018;**8**:537–55. https://doi.org/10.1158/2159-8290.CD-17-1461
157. Ibrahim YH, García-García C, Serra V *et al.* PI3K inhibition impairs BRCA1/2 expression and sensitizes BRCA-proficient triple-negative breast cancer to PARP inhibition. *Cancer Discov* 2012;**2**:1036–47. https://doi.org/10.1158/2159-8290.CD-11-0348
158. Juvekar A, Burga LN, Hu H *et al.* Combining a PI3K inhibitor with a PARP inhibitor provides an effective therapy for BRCA1-related breast cancer. *Cancer Discov* 2012;**2**:1048–63. https://doi.org/10.1158/2159-8290.CD-11-0336
159. Mo W, Liu Q, Lin CC-J *et al.* mTOR inhibitors suppress homologous recombination repair and synergize with PARP inhibitors via regulating SUV39H1 in BRCA-proficient triple-negative breast cancer. *Clin Cancer Res*

2016;**22**:1699–712. https://doi.org/10.1158/1078-0432.CCR-15-1772
160. Sun C, Fang Y, Yin J *et al.* Rational combination therapy with PARP and MEK inhibitors capitalizes on therapeutic liabilities in RAS mutant cancers. *Sci Transl Med* 2017;**9**:eaal5148. https://doi.org/10.1126/scitranslmed.aal5148
161. Vena F, Jia R, Esfandiari A *et al.* MEK inhibition leads to BRCA2 downregulation and sensitization to DNA damaging agents in pancreas and ovarian cancer models. *Oncotarget* 2018;**9**:11592–603. https://doi.org/10.18632/oncotarget.24294
162. Konstantinopoulos PA, Barry WT, Birrer M *et al.* Olaparib and α-specific PI3K inhibitor alpelisib for patients with epithelial ovarian cancer: a dose-escalation and dose-expansion phase 1b trial. *Lancet Oncol* 2019;**20**:570–80. https://doi.org/10.1016/S1470-2045(18)30905-7
163. Batalini F, Xiong N, Tayob N *et al.* Phase 1b clinical trial with alpelisib plus olaparib for patients with advanced triple-negative breast cancer. *Clin Cancer Res* 2022;**28**:1493–9. https://doi.org/10.1158/1078-0432.CCR-21-3045

Received: October 17, 2024. **Revised:** February 13, 2025. **Editorial Decision:** February 14, 2025. **Accepted:** March 4, 2025